UNIVERSIDADE FEDERAL DE JUIZ DE FORA
FACULTY OF ENGINEERING
ELECTRICAL ENGINEERING – ELECTRONIC SYSTEMS

Luan Gomes Mattosinhos de Carvalho

Characterization and simulation of photomultiplier tube signals for the CYGNO experiment

Juiz de Fora
2025

Luan Gomes Mattosinhos de Carvalho

Characterization and simulation of photomultiplier tube signals for the CYGNO experiment

Final undergraduate thesis presented to the Faculty of Engineering at the Federal University of Juiz de Fora as a partial requirement for obtaining a Bachelor's degree in Electrical Engineering – Electronic Systems.

Advisor: Prof. Dr. Rafael Antunes Nóbrega

Juiz de Fora

2025

Ficha catalográfica elaborada através do Modelo Latex do CDC da UFJF
com os dados fornecidos pelo(a) autor(a)

Carvalho, Luan Gomes Mattosinhos de.
Characterization and simulation of photomultiplier tube signals for the CYGNO experiment / Luan Gomes Mattosinhos de Carvalho. – 2025.
78 f. : il.

Advisor: Rafael Antunes Nóbrega
Trabalho de Conclusão de Curso (graduação) – Universidade Federal de Juiz de Fora, Faculty of engineering. Electrical Engineering – Electronic Systems, 2025.

1. Dark matter detection. 2. Particle physics experiment. 3. Photomultiplier tube. 4. Noise analysis. 5. Signal simulation. I. Nóbrega, Rafael Antunes, adv. Título.

Luan Gomes Mattosinhos de Carvalho

Characterization and simulation of photomultiplier tube signals for the CYGNO experiment

Final undergraduate thesis presented to the Faculty of Engineering at the Federal University of Juiz de Fora as a partial requirement for obtaining a Bachelor's degree in Electrical Engineering – Electronic Systems.

Approved at 17 of March of 2025

EXAMINATION BOARD

Prof. Dr. Rafael Antunes Nóbrega - Advisor
Universidade Federal de Juiz de Fora

Prof. Dr. Augusto Santiago Cerqueira
Universidade Federal de Juiz de Fora

Dr. David de Melo Souza
Universidade Federal de Juiz de Fora

Dedico este trabalho aos meus pais, irmã, familiares e amigos.

ACKNOWLEDGEMENT

Agradeço profundamente aos meus pais pelo amor, apoio, suporte e dedicação ao longo de toda a minha jornada. À minha irmã, pelo carinho e compreensão constantes.

Aos meus professores, pela orientação e contribuições essenciais à minha formação.

Aos meus amigos e companheiros da faculdade, Augusto, Bernardo, Elian, Luís e Otton, pela amizade e companheirismo durante todo o processo.

Ao Igor Pains e Mariana, e demais colegas do NIPS, por terem sido essenciais para o desenvolvimento deste trabalho.

Ao meu professor orientador, Rafael, pela paciência, conselhos valiosos e apoio ao longo do desenvolvimento deste trabalho, além de todas as oportunidades que me foram concedidas.

Ao Giovanni Mazzitelli e Igor Abritta, juntamente com meu orientador, pela oportunidade de poder visitar pessoalmente a colaboração e o experimento CYGNO.

Por último, um agradecimento especial ao CNPq (Conselho Nacional de Desenvolvimento Científico e Tecnológico), à Universidade Federal de Juiz de Fora, à Faculdade de Engenharia e ao Instituto Nazionale di Fisica Nucleare (INFN), por todo suporte e apoio para o desenvolvimento deste trabalho.

RESUMO

O experimento CYGNO emprega técnicas de leitura óptica em detectores gasosos para aumentar a sensibilidade na busca direta por matéria escura. Um componente crítico desse método de detecção é a caracterização e simulação precisa dos sinais de tubos fotomultiplicadores (PMT). Os PMTs desempenham um papel fundamental na reconstrução tridimensional da trajetória da partícula, o que é crucial para determinar a direcionalidade do evento, e servem como um parâmetro para estimativa de energia e seleção de eventos. Neste contexto, o desenvolvimento de uma simulação permite a exploração de diferentes configurações experimentais, incluindo condições que podem ser desafiadoras de reproduzir em laboratório. Este estudo apresenta uma metodologia para modelar sinais de PMTs, caracterizando respostas de fotoelétrons individuais, analisando contribuições de ruído eletrônico e validando a simulação por meio de análise comparativa com dados experimentais. Utilizando a configuração experimental do CYGNO, avaliamos propriedades do sinal, como ganho, densidade espectral de ruído e características temporais, garantindo a confiabilidade das formas de onda simuladas. Os resultados demonstram uma forte correlação entre os sinais simulados e reais, confirmando a eficácia do modelo desenvolvido na reprodução de observações experimentais.

Palavras-chave: detecção de matéria escura; experimento de física de partículas; tubo fotomultiplicador; análise de rúido; simulação de sinal.

ABSTRACT

The CYGNO experiment employs optical readout techniques in gaseous detectors to enhance sensitivity in direct dark matter searches. A critical component of this detection method is the precise characterization and simulation of photomultiplier tube (PMT) signals. The PMTs play a fundamental role in the three-dimensional reconstruction of the particle's trajectory, which is crucial for determining event directionality, and serve as a parameter for energy estimation and event selection. In this context, the development of a simulation allows the exploration of different experimental configurations, including conditions that may be challenging to reproduce in the laboratory. This study presents a methodology for modeling PMT signals by characterizing single photoelectron responses, analyzing electronic noise contributions, and validating the simulation through comparative analysis with experimental data. By leveraging the CYGNO experimental setup, we evaluate signal properties such as gain, noise spectral density, and time characteristics, ensuring the reliability of the simulated waveforms. The results demonstrate a strong correlation between simulated and real PMT signals, confirming the effectiveness of the developed model in reproducing experimental observations.

Keywords: dark matter detection; particle physics experiment; photomultiplier tube; noise analysis; signal simulation.

LIST OF ILLUSTRATIONS

LIST OF TABLES

LIST OF ABBREVIATIONS AND ACRONYMS

TPC	Time Projection Chamber
PMT	Photomultiplier Tube
DM	Dark Matter
WIMP	Weakly Interacting Massive Particle
LHC	Large Hadron Collider
SMP	Standard Model Particle
NR	Nuclear Recoil
MPGD	Micro Pattern Gas Detector
MWPC	Multi-Wire Proportional Chamber
GEM	Gas Electron Multiplier
T.T.S	Transit Time Spread
FWHM	Full Width at Half Maximum
LNGS	Laboratori Nazionali del Gran Sasso
LIME	Long Imaging Module Experiment
sCMOS	Scientific CMOS
EMG	Exponentially Modified Gaussian
PDF	Probability Density Function
PSD	Power Spectral Density
AR	Autoregressive
MA	Moving average
ARMA	Autoregressive-moving-average
DFT	Discrete Fourier transform
ADC	Analog-to-Digital Converter
SPE	Single Photoelectron
LPG	Light Pulse Generator
SNR	Signal-to-noise ratio

CONTENTS

1 INTRODUCTION

The study of dark matter (DM) remains one of the most significant challenges in modern physics. The CYGNO experiment (1), part of the CYGNUS collaboration, employs gaseous detectors with optical readout to investigate interactions of hypothetical particles, such as Weakly Interacting Massive Particles (WIMPs) (2). To ensure the reliability of measurements and the accuracy of collected data, it is essential to understand and model the signals generated by photomultiplier tubes (PMTs), which play a central role in detecting low-light events.

In the context of the CYGNO experiment, the PMTs play a crucial role by detecting very weak light signals generated by particle interactions within the gaseous detector. While the optical sensor camera captures and stores information in two dimensions, the PMT provides the third dimension through its temporal behavior, which is essential for the three-dimensional reconstruction of particle trajectories. This capability is vital for determining the direction of the particles and estimating the energy involved in the interactions. Furthermore, PMTs are fundamental for resolving events in both time and space, which is crucial for precise event selection and background rejection.

Electrical engineering is fundamental in this context, providing instrumentation, sensing, and simulation techniques to characterize the electrical signals produced by the detectors. A detailed analysis of PMT responses, including parameters such as quantum efficiency, gain, and noise spectral density, not only optimizes sensor performance but also validates the methodology employed in the experiment.

This study focuses on developing a simulation model for the PMT signals used in CYGNO, with the goal of accurately reproducing the characteristics observed in experimental data. Validation is performed through a detailed comparison with real data, ensuring the model's applicability in improving signal detection and analysis. The results contribute to advancing PMT-based detection techniques and highlight the importance of computational modeling in experimental physics.

To provide a comprehensive understanding of the study, this document is structured as follows: Chapter 2 provides a literature review on dark matter detection techniques, with an emphasis on the role of photomultiplier tubes. Chapter 3 introduces the CYGNO experiment, detailing its methodology and research objectives. Chapter 4 describes the methodology used in this study, including data acquisition, noise analysis, and signal processing techniques. Chapter 5 presents the characterization of PMT signals, highlighting single photoelectron response analysis and gain estimation. Chapter 6 discusses the achieved results, comparing simulated and experimental data. Finally, Chapter 7 concludes the study, summarizing the findings and suggesting directions for future research.

2 LITERATURE REVIEW

The detection of dark matter is a key challenge in modern physics, requiring highly sensitive instruments and innovative techniques. This chapter explores the fundamental principles behind dark matter searches, with a focus on direct detection methods and the role of photomultiplier tubes in signal acquisition.

2.1 DARK MATTER DIRECT DETECTION

Over the last century, scientists and researchers have made significant efforts to develop a model that could explain elementary particles and their interactions, in order to understand everything observable in the universe. This effort led to the gradual development of the Standard Model of particle physics. The Standard Model is widely recognized for its ability to accurately describe nearly all empirical data collected from experiments related to high-energy physics and astronomy, for example. However, some exceptions have been discovered (3).

One such exception stems from the compelling evidence that most of the mass in the observable universe is not composed of the particles known and present in the Standard Model. As a result, astronomers proposed the existence of a hypothetical form of matter called dark matter nearly a century ago. Dark matter is invisible across the entire electromagnetic spectrum (4) and has become the standard paradigm in cosmology due to its influence and role in driving the evolution and shaping the landscape of our universe (5). Furthermore, it is estimated that dark matter is five times more abundant than baryonic matter and has fundamentally shaped the observable universe we see today.

To incorporate dark matter into the theoretical framework of particle physics, several models have been developed to explain it ((6), (7), (8), (9), (10)). The most widely accepted models are those based on the interactions of so-called Weakly Interacting Massive Particles.

The direct detection of these particles, aimed at determining their properties such as mass, coupling, and interaction cross-section, can currently be achieved through three main approaches:

- Identifying dark matter particles produced in hadron colliders, such as the Large Hadron Collider (LHC).
- Observing the decay of dark matter through annihilation processes, particularly in regions with a high dark matter density.
- Direct detection of WIMPs through scattering processes in highly sensitive experiments, such as CYGNO, which operate with extremely low background noise.

The possibility of directly detecting dark matter particles through WIMP interactions was first proposed in 1985. Since these particles carry no electric charge, their interaction with atomic electrons is highly improbable. However, elastic scattering with the atomic nucleus may occur, resulting in nuclear recoil (NR), which is detectable due to momentum transfer. The total energy loss associated with this recoil in a WIMP detector can be described by the following equation:

$$\left(\frac{dE}{dx}\right)_{tot} = \left(\frac{dE}{dx}\right)_{elec} + \left(\frac{dE}{dx}\right)_{nucl} \tag{2.1}$$

During the interaction between a WIMP and a nucleus, most of the dissipated energy is converted into heat, potentially leading to atomic excitation. The remaining energy is transferred through electronic losses, which can ionize or excite atoms, resulting in the emission of scintillation light. This light can be detected by photosensors. However, due to the low intensity of the generated signal, the number of photons available for detection is extremely limited.

2.1.1 Event signatures and backgrounds

Radiation interacting with the material in dark matter detectors can produce two main types of signatures: nuclear recoils and electronic recoils (ER). For example, electronic recoils will tend to occur because of the scattering between charged particles and atomic electrons. On the other hand, nuclear recoils happen exclusively when particles like neutrons collide with atomic nuclei, transferring energy to the nucleus, similar to the expected signals from WIMPs.

Still, background radiation can also induce these recoils, complicating the identification of DM signals. Cosmic rays are a large background radiation source. Primary cosmic rays are high-energy particles, primarily protons and light nuclei, originating from astrophysical sources. When primary rays collide with atmospheric particles, secondary rays are produced, such as X-rays, muons, pions, and neutrons.

Another source of background radiation is internal radioactivity. The materials used in the detector construction can have unstable isotopes, such as uranium, thorium, and potassium, that are radioactive and decay, emitting radiation. The decays produce background events and complicate it to distinguish these events from a potential DM signal.

2.1.2 Detectors for WIMPS Searches

In contemporary direct dark matter detection experiments, researchers seek to gain insight into the nature of dark matter by studying collisions between known particles, described by the Standard Model of particle physics, and dark matter candidates such as

WIMPs. These collisions, illustrated in Figure 1, result in the emission of two particles: one representing the WIMP and the other belonging to the Standard Model. During these interactions, the Standard Model particle can ionize atoms in the medium, and as the ionized material returns to its ground state, photons are produced. These emitted photons can be detected using photosensors, as is the case in the Xenon experiment (12).

Figure 1 – Simplified diagram of direct detection. DM particles interact with one Standard Model Particle (SMP), resulting in another particle of DM and another of the standard model

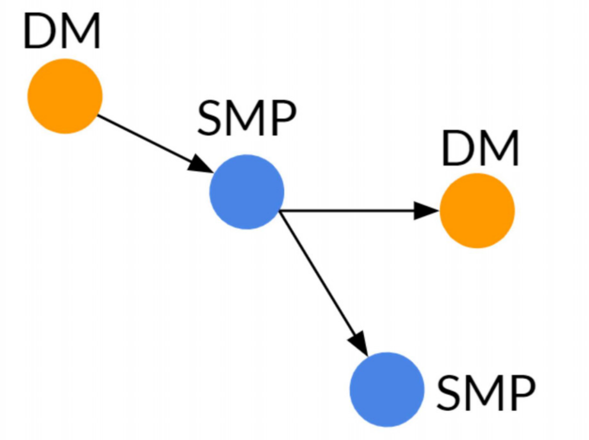

Source: Extracted from (11)

Numerous detectors have been developed worldwide with various designs to detect WIMP particles, which can be categorized as follows:

- **Inorganic Crystal Detectors:** These detectors use high-purity crystals to capture dark matter-induced charge signals. Early experiments used a 0.72kg Germanium crystal (13), later evolving to Silicon-based detectors like DAMIC (14) and SENSEI (15), improving sensitivity at lower masses. DAMA/LIBRA (16) and COSINE-100 (17) use NaI(Tl) scintillators to observe annual modulation.
- **Cryogenic Detectors:** Detecting dark matter through temperature shifts, these detectors operate at $\leq$ 50 mK, with most energy released as phonons (18). Key experiments include EDELWEISS (19) and CDMS (20).
- **Noble Liquid Detectors:** Using liquid noble gases (argon or xenon), these detectors measure scintillation and ionization signals in single or dual-phase setups with PMTs. Examples: DarkSide-50 (21), DEAP (22), LUX (23), and XENON10 (24).
- **Bubble Chambers:** Superheated liquids (e.g., CF3I, C3F8, C4F10) serve as WIMP targets. Particle interactions create bubbles, tracked via cameras for 3D

reconstruction and acoustic discrimination. Experiments: PICASSO ((25), (26)), PICO-2L (27) with a 3.3 keV threshold, PICO-60 (28), and COUPP (29).

- **Directional Detectors:** These detectors seek to determine WIMP directionality, distinguishing signals from background noise. Gas-based Time Projection Chamber (TPC) detectors reconstruct ionization tracks to identify recoil direction. Along with CYGNO, experiments such as MIMAC (30) and DRIFT-II (31) also fall into this category.

2.1.3 Time Projection Chamber

A Time Projection Chamber is a type of particle detector that utilizes a combination of electric and magnetic fields, along with a sensitive gas or liquid volume, to reconstruct in three dimensions the trajectory left by a particle interaction. The first TPC was developed by the American physicist David R. Nygren in the late 1970s at the Lawrence Berkeley Laboratory (32). This detector plays a fundamental role in particle physics experiments, offering high-precision reconstruction of charged particle interactions with the gas mixture and providing detailed information about their trajectories and energy deposition.

A typical TPC consists of a cylindrical or rectangular chamber filled with a carefully selected gas mixture, such as a noble gas or a combination of noble gases, which enables ionization when charged particles pass through. The chamber features an anode and a cathode positioned at opposite ends, as well as finely segmented electrodes, such as wire planes or readout pads, that register ionization signals. In modern TPCs, the signal amplification and readout processes rely on Micro Pattern Gas Detectors (MPGD), replacing the traditional Multi-Wire Proportional Chamber (MWPC) technology.

The TPC operates based on the following principle: If a charged particle passing through the gas has enough energy to ionize it, a track of electrons and ions is produced. Due to the electric field, electrons drift towards the anode, while ions migrate towards the cathode. The charge measured at the anode is expected to be proportional to the energy loss of the particle (33). The schematic representation of a TPC and its operation is illustrated in Figure 2.

The three-dimensional reconstruction can be done as follows:

- The x and y coordinates are determined directly from the readout of the segmented plane, achieving a resolution of just a few micrometers (μm).
- If the electron drift velocity (v_d) is known, the z-coordinate can be inferred using Equation (2.2), where t_0 is the interaction time and t_1 the electron arrival time at the anode.

Figure 2 – Schematic and working principle of a TPC

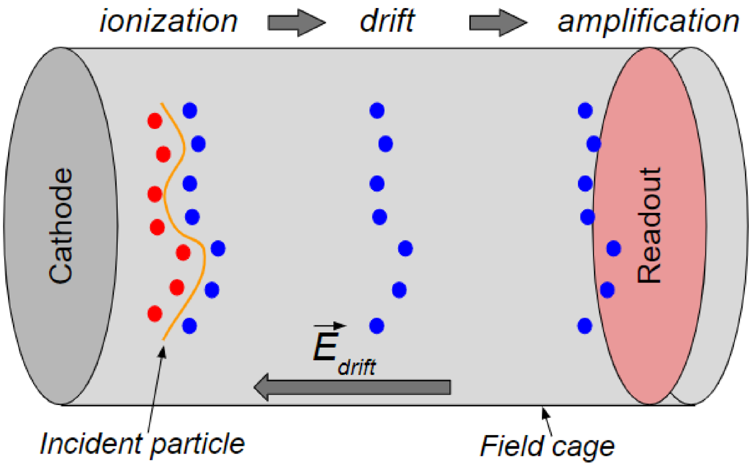

Source: Extracted from (11)

- If t_0 is unknown, it is still possible to reconstruct the z-coordinate, provided that the time resolution is sufficiently high to distinguish the arrival times of electrons originating from the same track.

$$z = v_d \times (t_1 - t_0) \tag{2.2}$$

Additionally, the charge collected at the anode (or cathode) is typically proportional to the ionization energy loss (dE/dx) of the incident particle. This measurement is a key parameter for particle identification, allowing different particle types to be distinguished based on their characteristic energy loss.

2.1.3.1 Diffusion effect

In TPCs, diffusion is a phenomenon that occurs when ionization electrons and positive ions drift toward the anode or cathode under the influence of an electric field (34). As these charged particles move through the gas volume, they interact with gas atoms, leading to both longitudinal and transverse diffusion.

Longitudinal diffusion refers to the spreading of electrons along the direction of the electric field, which is parallel to the TPC axis. Transverse diffusion corresponds to the spreading of electrons perpendicular to the electric field direction.

After drifting over a distance z, transverse and longitudinal profiles of the generated electron clouds can be described by Gaussian distributions, with standard deviations given by:

$$\sigma_{\mathrm{T}} = \sqrt{\sigma_{\mathrm{T0}}^2 \oplus D_{\mathrm{T}}^2 \cdot z} \tag{2.3}$$

$$\sigma_{\mathrm{L}} = \sqrt{\sigma_{\mathrm{L0}}^2 \oplus D_{\mathrm{L}}^2 \cdot z}, \tag{2.4}$$

where σ_{T0} and σ_{L0} are constant contributions due diffusion in the GEM structure and D_T and D_L are transverse and longitudinal diffusion coefficients that depend on the gas mixture and the electric field (35).

For gas mixtures of He/CF$_4$ in proportions of 60/40 and 70/30, the diffusion coefficient behavior for different electric field values is shown in Figure 3.

Figure 3 – Transverse and longitudinal diffusion coefficients for the two mixtures as a function of the electric field.

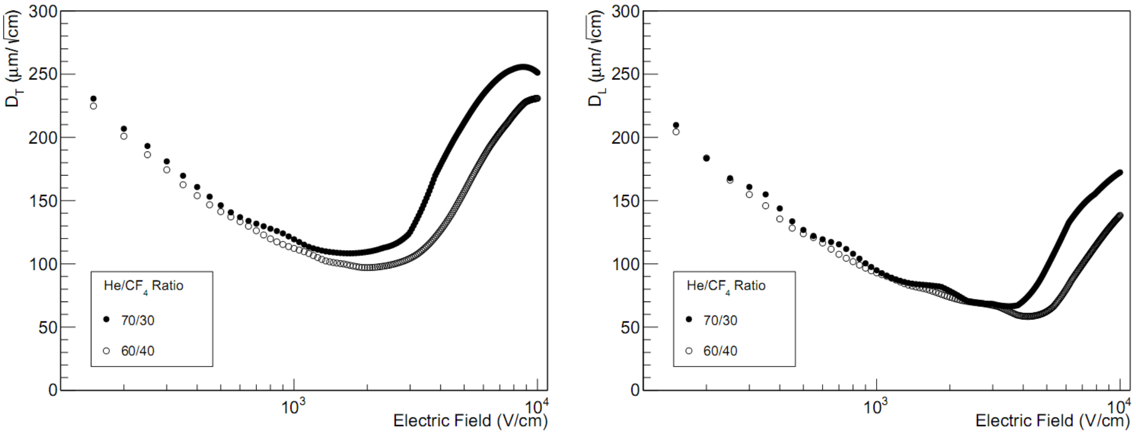

Source: Extracted from (35)

2.2 GAS ELECTRON MULTIPLIER

The Gas Electron Multiplier (GEM) is a type of gaseous ionization device first introduced in 1997 (36). It consists of very thin insulating sheet, typically made of Kapton, with a thickness of 50–70 μm, coated with copper on both sides. The foil is perforated with a large number of small holes, usually 30–50 micrometers in diameter, which are etched through the copper layers. These holes are arranged in a regular pattern, with a typical separation of approximately 140 micrometers.

When a charged particle passes through the GEM, it ionizes the gas molecules inside the holes, producing a significant number of electrons. These electrons are then accelerated by an electric field applied across the GEM, as illustrated in Figure 4, leading to an avalanche multiplication process as they pass through the holes. The gain achieved by a single GEM is directly proportional to the potential difference applied to it. The output of the GEM is typically acquired in two ways: by reading the signals induced on the electrodes or by detecting the light emitted during the de-excitation of the gas molecules. In the case of CYGNO, the light is recorded using an optical sensor placed on a readout plane positioned behind the GEM.

To achieve higher gains while operating at lower voltages, multiple GEM layers can be cascaded. Two or more GEM layers can be used in sequence, forming configurations

Figure 4 – Schematics and fields of the gas electron multiplier.

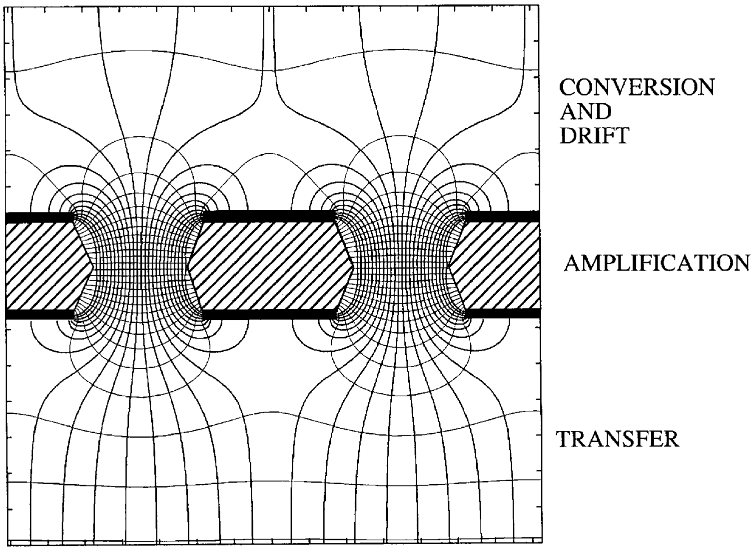

Source: Extracted from (37)

such as double-GEM, triple-GEM, or quad-GEM, among others. In multi-GEM detectors, the total gain is distributed across the layers, with each stage capable of achieving gains on the order of 10^6 (38). In fact, the triple-GEM configuration has become a standard in many applications ((39), (40), (41)), and it is the configuration adopted by the CYGNO experiment.

2.3 PHOTOMULTIPLIER TUBES

Photomultiplier tubes are vacuum-based devices widely used for detecting extremely low levels of light intensity. They consist of an input window, a photocathode, focusing electrodes, an electron multiplier composed of dynodes, and an anode sealed within an evacuated glass tube. Figure 5 illustrates the schematic construction of a PMT.

When light enters the tube through the input window, it excites the electrons in the photocatode, triggering the emission of photoelectrons into the vacuum through the photoelectric effect (44). The emitted photoelectrons are then accelerated and focused by focused electrodes toward the first dynode, where they are multiplied by means of secondary electron emission. This process is repeated at each dynode in the electron multiplier. In the final stage, a cluster of secondary electrons is emitted from the last dynode and reaches the anode, where it is collected and converted into an electrical signal.

Figure 5 – Schematic construction of a PMT

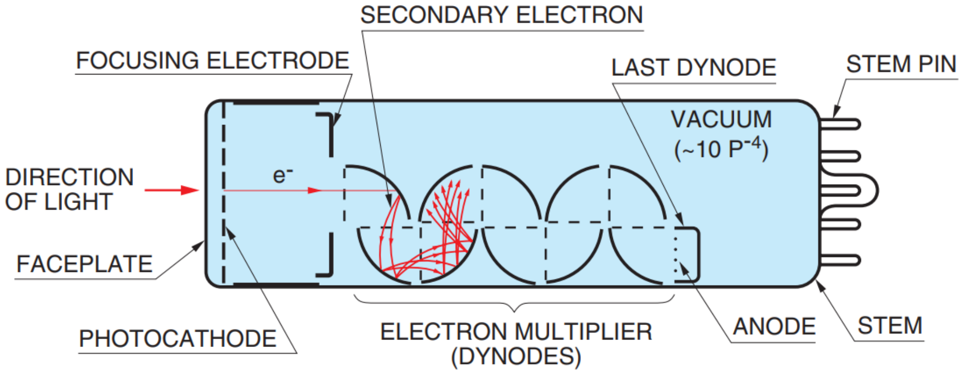

Source: Extracted from (42)

2.3.1 Time characteristics

The time response of a PMT is primarily determined by the transit time required for photoelectrons, emitted from the photocathode, to reach the anode after undergoing multiplication, as well as by the variations in transit time among individual photoelectrons (42).

Figure 6 illustrates the definitions of all concepts involved in this process.

The rise time is defined as the duration it takes for the output pulse to increase from 10% to 90% of its peak height, whereas the fall time is the time required for the pulse to decrease from 90% to 10% of its peak height.

The Transit Time Spread (T.T.S) represents the fluctuation in transit times for individual photoelectron pulses when the photocathode is fully illuminated by single photons. These fluctuations follow a Gaussian distribution, and their spread is typically characterized by the full width at half maximum (FWHM) of the probability distribution. The FWHM can be directly related to the standard deviation σ through the following equation:

$$\mathrm{FWHM} = 2\sqrt{2\ln 2}\,\sigma \approx 2.355\,\sigma \tag{2.5}$$

2.3.2 Detection efficiency

The detection efficiency of a PMT is defined as the ratio of the detected signal to the input signal of a photomultiplier tube. In photon counting this is expressed as the product of the photocathode quantum efficiency and the collection efficiency.

Quantum efficiency is the number of photoelectrons emitted from the photocathode divided by the number of incident photons, while collection efficiency is defined as the ratio of the number of pulses output from the anode to the number of photoelectrons

Figure 6 – Concept of time characteristics

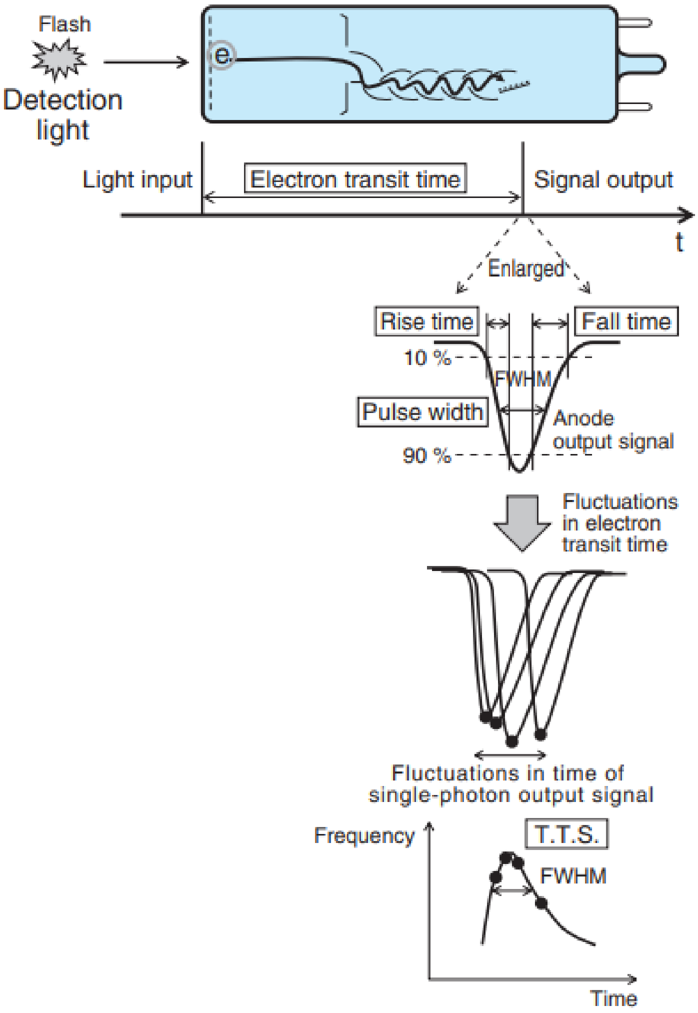

Source: Extracted from (42)

emitted from the photocathode. The curve of relative collection efficiency is typically plotted as a function of the voltage between the photocathode and the first dynode (42).

An example of detection efficiency is illustrated in Figure 7.

Figure 7 – Example of detection efficiency

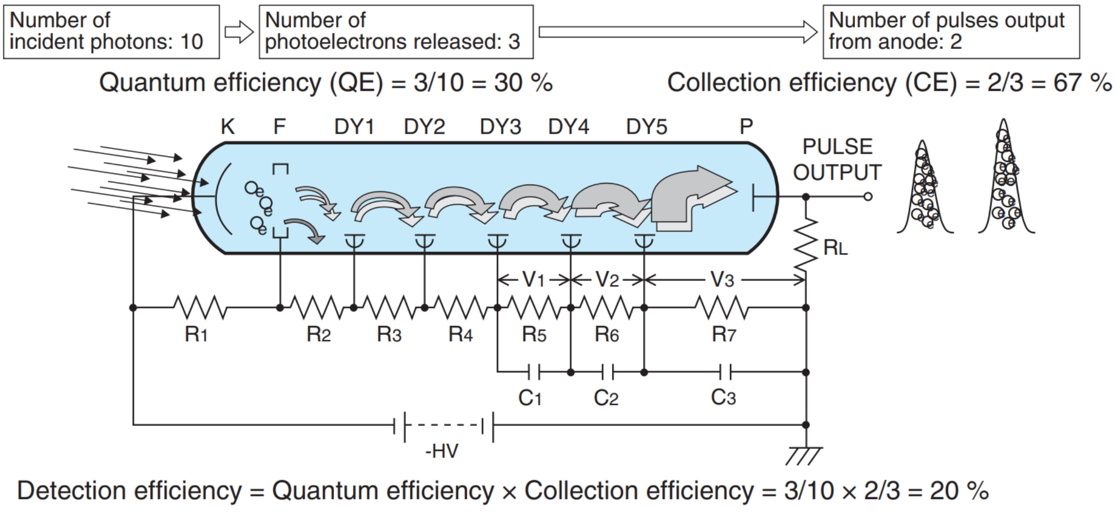

Source: Extracted from (42)

3 CYGNO

The CYGNO experiment (a CYGNus module with Optical readout) is part of the CYGNUS proto-collaboration, which aims at constructing a network of underground observatories for directional DM search. The experiment leverages optical readout technology with multiple-GEM structures in large-volume Time Projection Chambers to study rare events, such as interactions of low-mass dark matter particles or solar neutrinos. By integrating high-resolution sCMOS cameras with fast light sensors, the experiment enables precise 3D track reconstruction, achieving excellent energy resolution and exceptional sensitivity in the few-keV range. In addition, its advanced particle identification capabilities allow for effective discrimination between nuclear and electronic recoils, improving the reliability of signal detection.

Throughout this chapter, an overview of the CYGNO project will be provided, highlighting its research approach and how it is conducted.

3.1 DARK MATTER SEARCHES WITH CYGNO

The presence in the universe of large amounts of dark matter is well-established in modern physics, yet its nature remains elusive. WIMPs, electrically neutral particles with weak interactions and masses ranging from a few to thousands of GeV, are a strong DM candidate predicted by extensions of the Standard Model of particle physics and the Λ-CDM model of cosmology (43). Observations of galactic rotational curves suggest the existence of a DM halo, through which luminous matter moves. This motion creates a relative velocity between Earth-based detectors and DM particles, which can be exploited for detection via nuclear recoil events. In particular, low-energy (1–100 keV) nuclear recoils are expected to be the clearest evidence of WIMP interactions.

Direct DM detection in the GeV mass region faces the challenge of discrimination rare nuclear recoils from more common backgrounds. CYGNO leverages two key effects for signal identification: seasonal modulation and directional dependence. The Earth's motion around the Sun causes a small seasonal variation in detected DM rates, while the Earth's rotation leads to a much stronger diurnal modulation of the DM flux. The expected peak flux aligns with the Cygnus constellation, therefore directional measurements of the WIMP can provide a unique signature that background events cannot mimic. Additionally, they allow for discrimination between DM halo models and constraints on WIMP properties.

The CYGNO experiment aims to build a large direct directional detector of DM using a TPC with optical readout based on a Gas Electron Multiplier stack working with a He/CF_4 gas mixture at atmospheric pressure and room temperature in order to study rare events with energy releases in the range between hundreds of eV up to tens of keV.

The usage of a He/CF_4 gas mixture (60/40) increases sensitivity to WIMPs, enhancing detection while preserving directional information and helping to reject low-energy background noise. To further improve sensitivity, an amplification stage based on MPGD was adopted, consisting of microelectronic structures with distances smaller than 1 mm between the cathode and anode. GEM technology is employed for charge pre-amplification.

All of these features enable the experiment to explore new frontiers in particle physics, particularly in the need to discriminate low-energy nuclear recoils and gather information related to the directionality of these particles.

3.1.1 CYGNO ROADMAP

The CYGNO project follows a phased development strategy aimed at optimizing the apparatus, enhancing its performance, and managing unexpected costs effectively. The roadmap consists of three key phases:

- **PHASE_0:** deployment of a 50-liter prototype at the INFN-Laboratori Nazionali del Gran Sasso (LNGS). This phase has been successfully completed, and the present work is based on its results.
- **PHASE_1:** testing the scalability of the experimental approach with a $\mathcal{O}(1)$ m^3 detector.
- **PHASE_2:** proposal of a larger-scale experiment (30–100 m^3) to explore the 1–10 GeV WIMP mass range.

Figure 8 illustrates the entire CYGNO experiment roadmap.

Figure 8 – CYGNO experiment roadmap

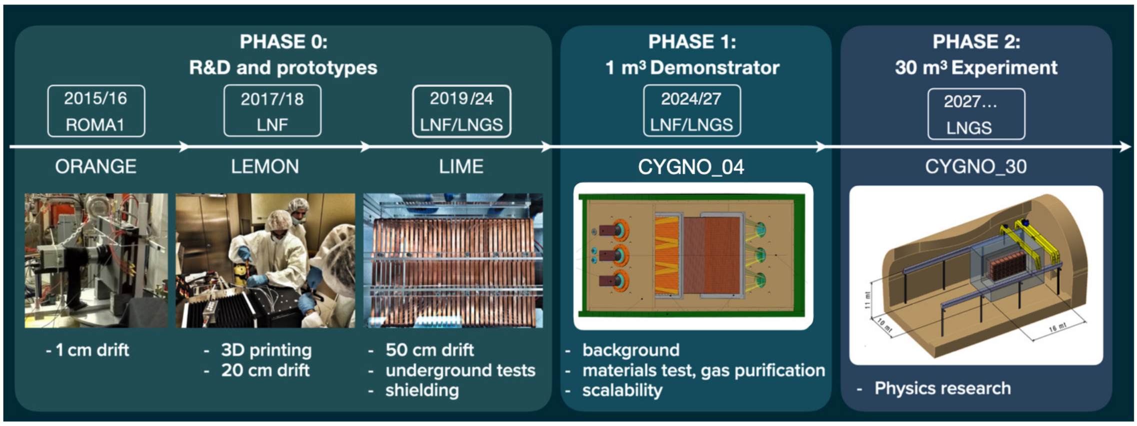

Source: Extracted from CYGNO Collaboration (2024).

3.2 LIME PROTOTYPE

The Long Imaging ModulE (LIME) detector is the larger prototype foreseen to conclude the PHASE_0 of the CYGNO project. It has a volume of 50 L and features a structure composed of 34 copper rings with an electron collection area of 33×33 cm^2. Additionally, it includes a thin Triple-GEM, which amplifies the charge produced in the drift region, extending 50 cm in length.

The detector is filled with a gas mixture of He (60%) and CF_4(40%) at atmospheric pressure, enclosed in a 10 mm thick plexiglass box that provides gas tightness. A drift field of approximately 1 kV/cm is established by applying a 50 kV potential across the electrodes.

A Hamamatsu ORCA Fusion sCMOS camera (2304 × 2304 pixels) is integrated with four PMTs, positioned at the corners of the readout area to detect secondary scintillation light. This setup enables 3D trajectory reconstruction of the particle while ensuring precise localization of the region of interest.

The LIME prototype schematic can be seen in Figure 9.

Figure 9 – Schematic of LIME prototype

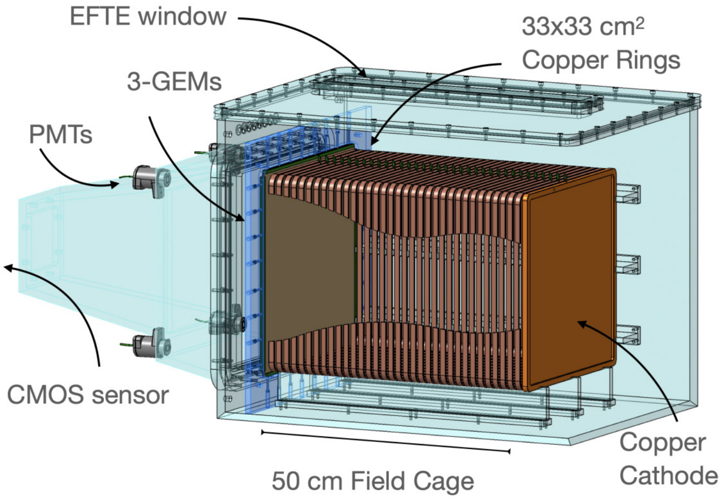

Source: Extracted from CYGNO Collaboration (2024).

3.2.1 PMT R7378A

The PMT model chosen by the CYGNO collaboration is the Hamamatsu Photomultiplier Tube R7378A (45). Details of its dimensions and structure are illustrated in the schematic shown in Figure 10. Figure 11 presents the curves of the typical spectral response and gain of this PMT. The typical time response characteristics are grouped in Table 1.

Figure 10 – PMT R7378A schematic

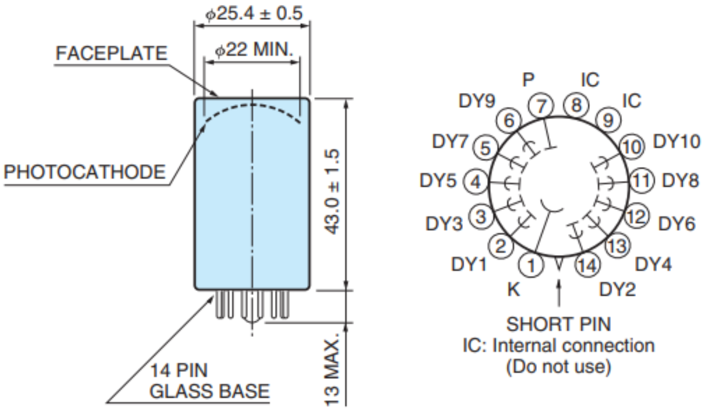

Source: Extracted from (45)

Figure 11 – PMT R7378A typical spectral response (left) and gain characteristics (right)

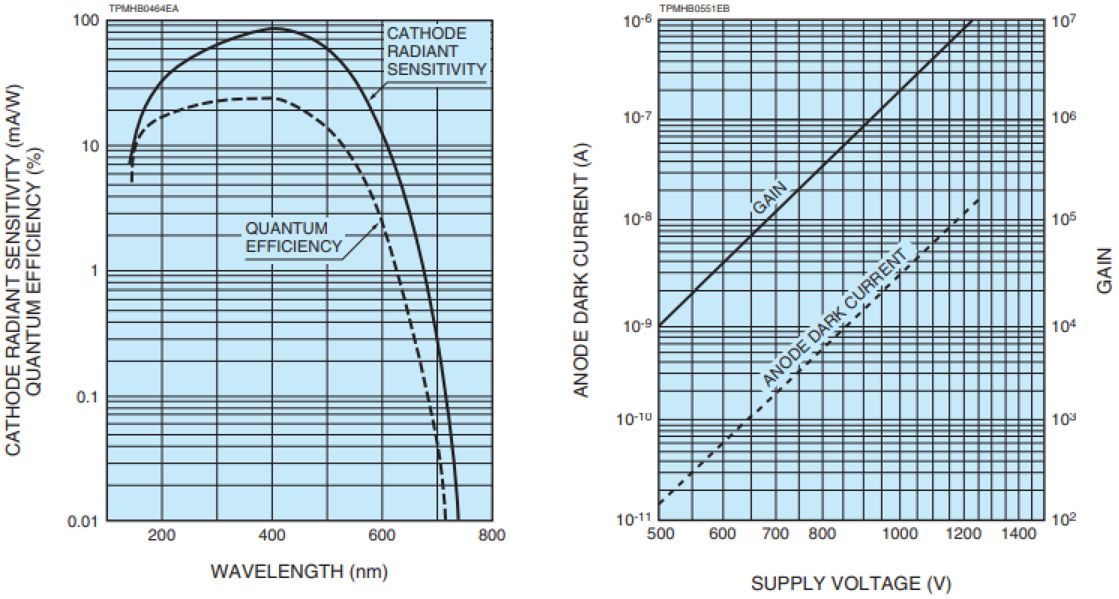

Source: Extracted from (45)

All of this information from the PMT datasheet will be used during the development of this work in order to validate the presented results.

3.2.2 Experimental setup

The LIME experimental setup consists of a centrally positioned sCMOS camera on the x-y plane, along with four PMTs. The GEM plane is the origin of the z-axis. Figure

Table 1 – PMT R7378A typical time response characteristics

Parameter	Value
Anode pulse rise time	1.5 ns
Electron transit time	17 ns
Transit time spread (T.T.S)	0.9 ns

Source: Prepared by the author (2024).

12 illustrates the positions of the PMTs on the x-y plane, with respect to the camera view and the GEM plane.

Figure 12 – PMT relative positions

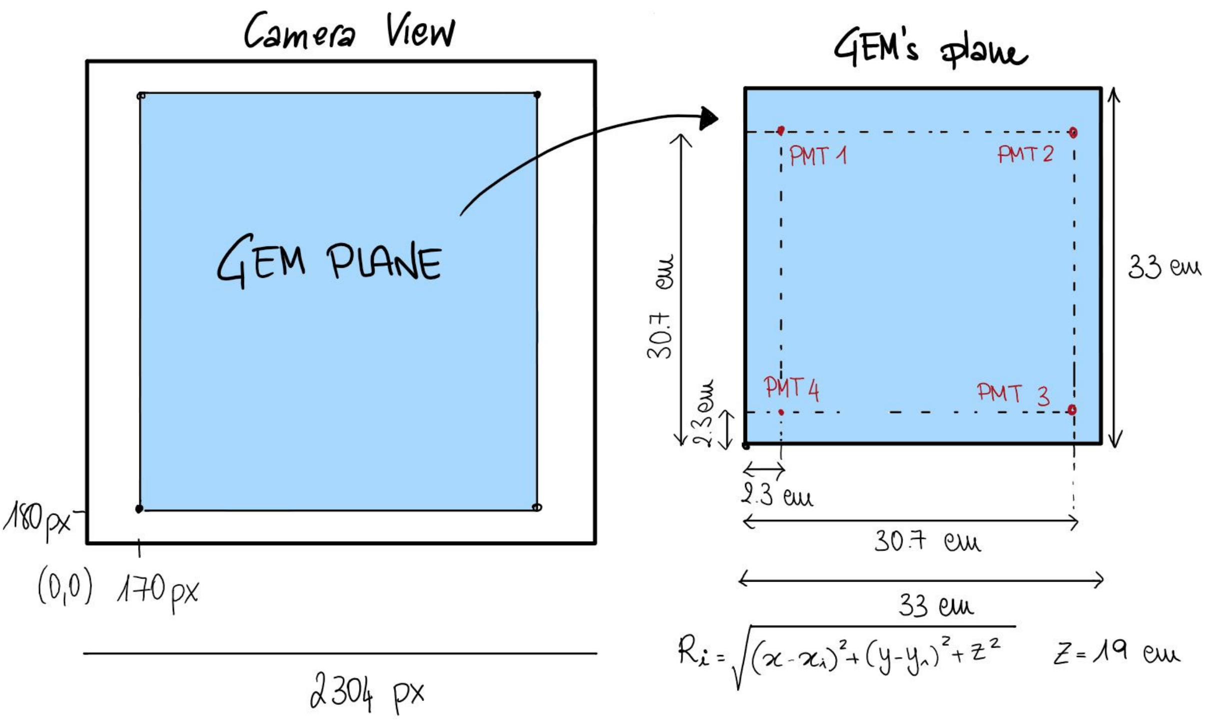

Source: Extracted from (46).

Table 2 presents detailed information about the four PMTs, including their relative positions in the three-dimensional plane and their respective supply voltages (50).

Additionally, to save signals generated by the PMTs with both short and long time extensions, the setup uses two digitizers, CAEN v1742 (47) and CAEN v1720 (48).

Table 2 – PMT positions and supply voltages.

	Position (x, y, z)	**Supply Voltage**
PMT 1	(23, 307, 190) mm	772 V
PMT 2	(307, 307, 190) mm	772 V
PMT 3	(307, 23, 190) mm	800 V
PMT 4	(23, 23, 190) mm	772 V

Source: Prepared by the author (2024).

Throughout this work, they will be referred to as the **Fast Digitizer** and **Slow Digitizer**, respectively, based on the time extensions. Each digitizer utilizes four of its available channels to connect to the four PMTs; channel 1 is connected to PMT 1, channel 2 to PMT 2, and so on. Further details on their technical specifications and the configurations used in the setup can be found in Table 3.

Table 3 – Fast and Slow digitizers specifications

	Resolution	**Sampling Rate**	**Window length**	**Time window**
CAEN v1742	12 bit	750 MS/s	1024 Samples	1.365 μs
CAEN v1720	12 bit	250 MS/s	4000 Samples	16 μs

Source: Prepared by the author (2024).

3.2.3 Daily calibration with ^{55}Fe source

The CYGNO collaboration conducted several data acquisitions using an external radioactive source of ^{55}Fe. For each acquisition, 100 camera images are saved, along with the PMT waveforms collected by digitizers corresponding to each image. These acquisitions are referred to as "runs."

The ^{55}Fe runs are intended to perform a z-scan with the ^{55}Fe source to evaluate the current light yield and calibrate the energy scale. Since these runs were conducted daily, they were part of the so-called **Daily Calibration**.

The z-scan is performed at five different positions, each referred to as a Step, with the following values:

- Step 1: z = 50 mm

- Step 2: z = 151 mm
- Step 3: z = 251 mm
- Step 4: z = 351 mm
- Step 5: z = 466 mm

The signals generated in the GEM from the ^{55}Fe source, due to gas ionization, fall into the category of ER events. These signals typically have an energy of 6 keV and appear as circular spots in the images captured by the camera. An example is shown in Figure 13, as follows.

Figure 13 – Image captured with ^{55}Fe events.

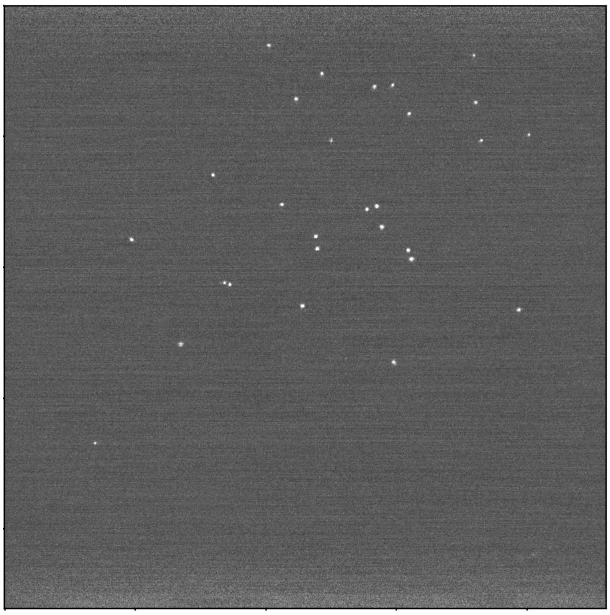

Source: Prepared by the author (2025).

4 METHODOLOGY

One of the main reasons the CYGNO collaboration uses PMTs in the experiment is due to the temporal behavior of the waveforms generated by these sensors.

The signals generated by the PMTs depend on the x-y positions where the electrons, produced in the detector, reach the Triple GEM plane. Additionally, the inclination of the incident particle relative to the GEM plane influences the duration of the signal, which aids in the 3D reconstruction of the event. Furthermore, the z-direction position where electron ionization occurs during the interaction with an external particle also influences the diffusion of this electron cloud, as described in Section *2.1.3.1*, which will affect the arrival times at the GEM and consequently the waveform generated by the PMTs.

The interactions inside the detector, including the behavior of the electron cloud and photon production, can be simulated using the LIME detector simulation software (49) developed by the collaboration. In addition, it is possible to simulate an image with a signal generated by the interaction of an external particle of a given energy. Users can define the x-y-z coordinates in the image, and the simulation output provides the electron arrival times at the GEM plane and the number of photons produced.

Given this context, the methodology to be adopted aims to use the output of the detector simulation as input for the PMT simulation. All aspects of this process will be discussed throughout this chapter.

4.1 PMT SIMULATION STRATEGY

As previously mentioned, the interaction of the gas with an external particle can induce ionization. This results in the formation of an electron cloud. In the three-dimensional context of the simulation, this cloud is represented by a grid of voxels. Each voxel will undergo diffusion in the z-direction and, upon reaching the GEM plane with a specific arrival time, will produce a certain number of photons.

Each photon will propagate from its position on the GEM plane to the PMT plane, with the probability of hitting one of the four sensors. If it hits, it may generate a photoelectron, and consequently a signal.

Thus, the PMT simulation will be based on the single photoelectron signals. Given the information on the number of produced photons at the GEM and their arrival times, the total waveform will be the composition of all single photoelectron signals generated individually by each of the photons.

Furthermore, it is important to remember that the signals generated are digitized by the Fast and Slow Digitizers, as mentioned in Section **3.2.2**. Consequently, the signals are subject to electronic noise, which may originate not only from the digitizers but also from the PMTs. This noise must be simulated and added to the PMT signal.

This entire fluxogram is illustrated in Figure 14, as follows:

Figure 14 – PMT Simulation fluxogram

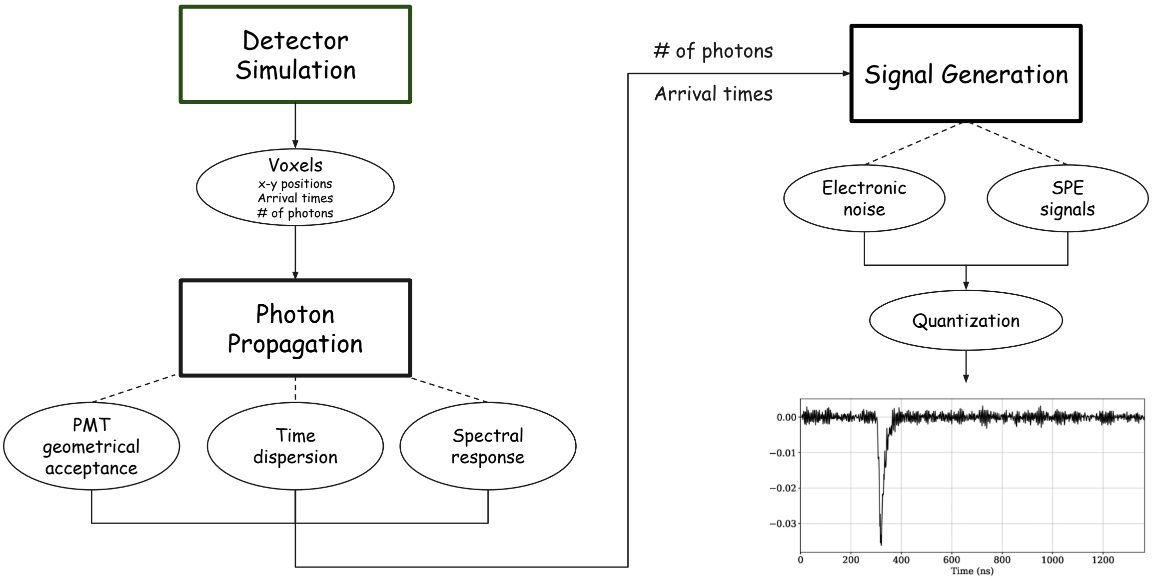

Source: Prepared by the author (2024).

4.2 PHOTON PROPAGATION

As photons travel from the GEM plane to the PMTs, their distribution and likelihood of detection depend on factors such as distance, geometrical acceptance and spectral response. Understanding these effects is essential for accurately modeling the signals detected by the PMTs and optimizing the overall performance of the simulation.

4.2.1 Geometrical acceptance

After being produced in the GEMs, light propagates towards the PMT plane, with the possibility of hitting the PMTs. The amount of light collected by the sensors depends on the system geometry.

Figure 15 presents a schematic representation of this problem. Initially, the four PMTs are not necessarily aligned perpendicularly to the light propagation vector. Therefore, it is necessary to consider the sensor's effective surface, which varies according to the spot position on the GEM plane. Additionally, the amount of collected light follows an inverse proportionality to $1/R$, where R is the distance between the spot on the GEM plane and the sensor's effective surface.

Figure 15 – Schematic drawing of the PMT geometrical acceptance.

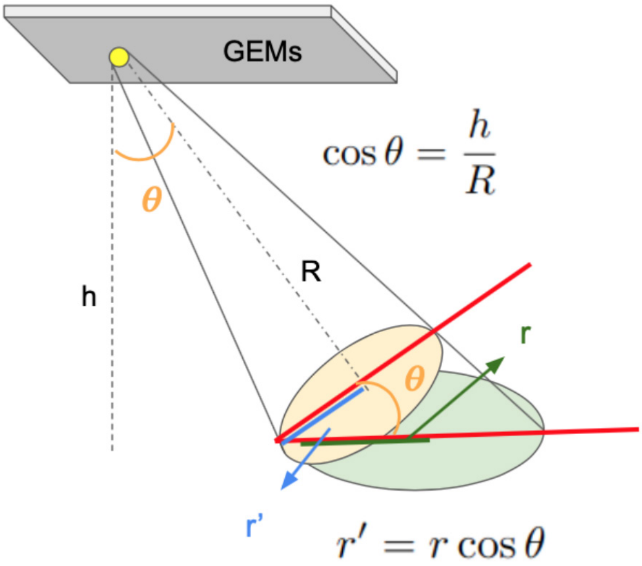

Source: Extracted from (50).

Following the schematic, the amount of light collected by each PMT is given by (see (50) for more details) :

$$L_i = \frac{L}{4R_i^2} \cdot \frac{r^2 h}{R_i}, \tag{4.1}$$

where:

- $i = 1, 2, 3, 4$ is the index of each PMT,
- $h = 190$ mm is the distance between the PMTs and the GEM plane (from Table 2),
- L is the light produced in the GEMs.

The equation above reveals a dependence on $1/R^3$. A study was conducted to validate this geometric dependence (51), and the results showed a closer, though not strictly exact, dependence on $1/R^4$, as seen in Figure 16.

Thus, the $1/R^\alpha$ dependence proved to be an uncertain measure. For this reason, in this work, α will be treated as a free parameter to tune the simulation. In the end, the optimal value of α will be evaluated and compared with those presented in this section.

Figure 16 – Charge variation as a function of the distance for the four PMTs.

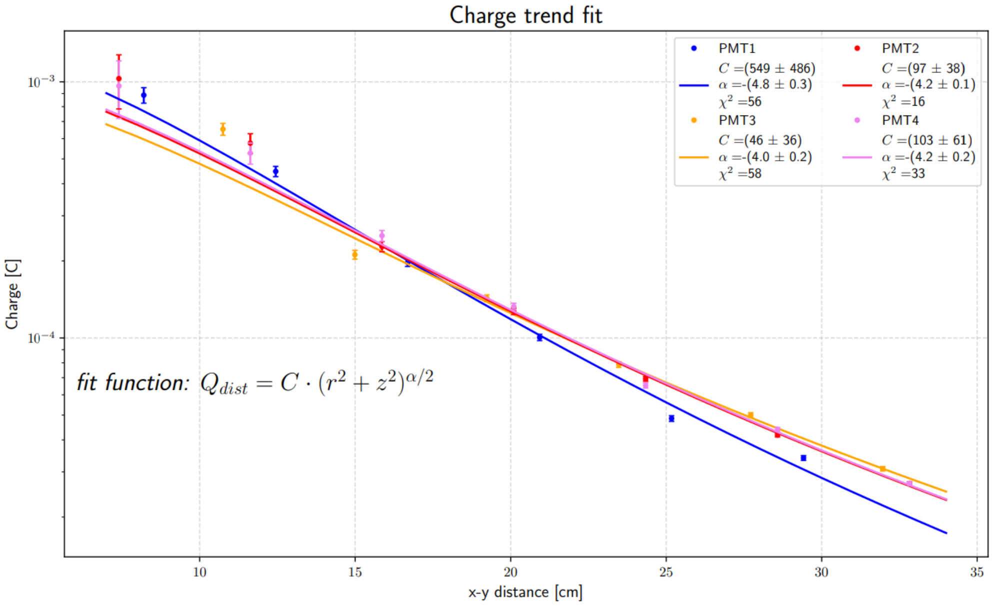

Source: Extracted from (51).

4.2.2 Time dispersion

To properly represent the temporal behavior of the PMT signals, it is necessary to consider the different factors contributing to its generation. The diffusion in the z-direction applied to the electron cloud follows a Gaussian distribution, as described in Section *2.1.3.1*, and when combined with the Transit Time Spread of the PMT, it results in an overall Gaussian temporal dispersion.

However, analysis of the typical waveforms of 55Fe events, as shown in Figure 17, reveals an additional exponential component. The origin of this exponential dispersion is likely due to the propagation of scintillation photons generated in the GEM as they travel towards the PMTs, extending the temporal spread beyond the known contributions.

To model both the Gaussian and exponential components of the time dispersion, a Exponentially Modified Gaussian (EMG) distribution can be used to fit the waveforms of 55Fe events. However, since the Gaussian components are already characterized, our interest lies in extracting the exponential parameter.

The EMG function is a widely used function to model the peak shape with exponential deviations in the tails of the central Gaussian (52). An EMG is obtained by the convolution of a Gaussian and a truncated exponential function.

The probability density function (PDF) of the EMG is defined as:

$$f(t;\mu,\sigma,\lambda) = \frac{\lambda}{2}\exp\left(\frac{\lambda}{2}(2\mu + \lambda\sigma^2 - 2t)\right)\operatorname{erfc}\left(\frac{\mu + \lambda\sigma^2 - t}{\sqrt{2}\sigma}\right), \tag{4.2}$$

Figure 17 – Typical PMT waveform of a 55Fe event

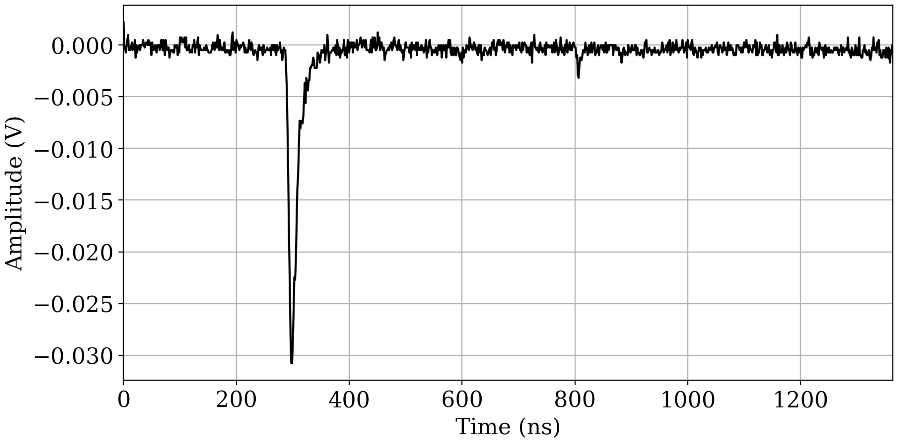

Source: Prepared by the author (2024).

where:

- μ represents the mean of the Gaussian component.
- σ is the standard deviation of the Gaussian component.
- λ is the rate parameter of the exponential component.
- erfc is the complementary error function.

To characterize λ, a dataset of waveforms generated from 55Fe spots was selected, and each waveform was fitted using the EMG function. An example of this procedure is illustrated in Figure 18.

The result obtained for the λ parameter is shown in Figure 19.

4.2.3 Spectral response

Photons are generated in the GEM using a He/CF_4 (60/40) gas mixture and travel through the air to the PMTs, passing through the glass structure of the LIME detector. The generation of a photoelectron at the PMT depends on its quantum efficiency.

To evaluate the fraction of photons that successfully generate a photoelectron, an analysis of the spectral response was performed. This analysis take into account the transmission properties of the LIME plexiglass structure and the quantum efficiency of the PMT R7378A (see Figure 11). The spectrum is presented in Figure 20, while Table 4 highlights the results, detailing the influence of each curve on the spectrum of the generated photons.

Figure 18 – Example of the λ characterization procedure

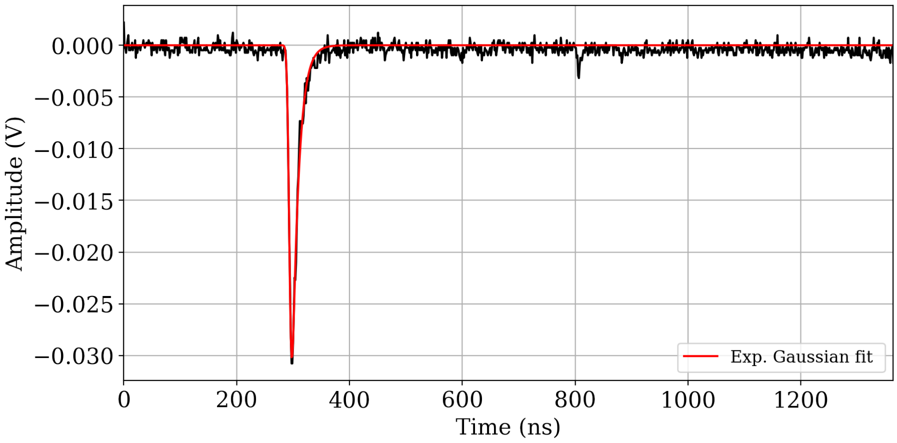

Source: Prepared by the author (2024).

Figure 19 – λ distribution histogram

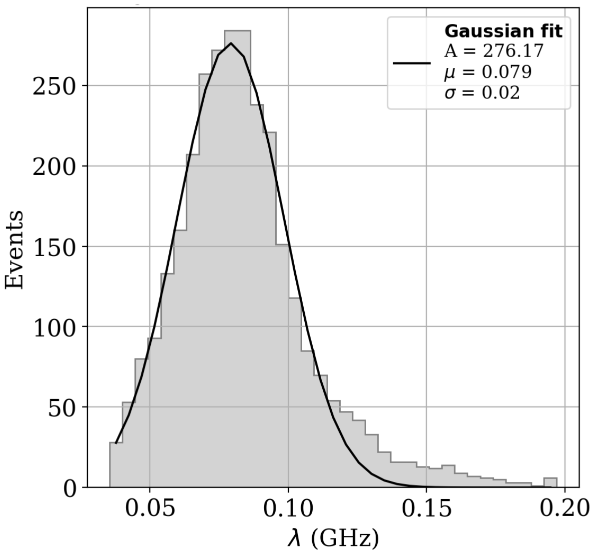

Source: Prepared by the author (2024).

From the spectrum of the generated photons, two main peaks are observed: the first, larger peak in the high-frequency region (200 - 350 nm), and a smaller peak in the low-frequency region (550 - 800 nm).

The results of the analysis show that the combination of the PMT R7378A and Plexiglass transmission significantly reduces the fraction of photons. This occurs because the quantum efficiency of the PMT suppresses the second peak of the photon spectrum, while the transmission properties of Plexiglass eliminate the first peak.

Figure 20 – Eletromagnetic spectrum of Photon Propagation and Detection

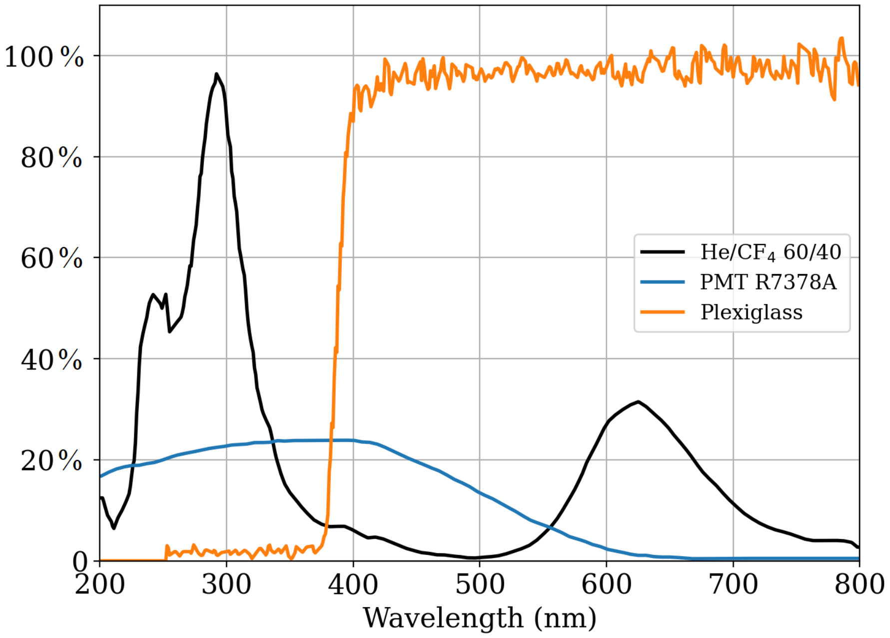

Source: Prepared by the author (2024).

Table 4 – Fraction of photons that successfully generate a photoelectron

Combination	Fraction of photons
PMT R7378A	15.03%
Plexiglass	36.42%
PMT R7378A + Plexiglass	1.36%

Source: Prepared by the author (2024).

4.3 SIGNAL GENERATION

This section will cover the simulation process of the signals generated by the PMTs and collected by the digitizers, following the photon propagation stage.

4.3.1 Noise generation

Accurate simulation of the electronic noise from the PMT signals is crucial to maintaining the fidelity of the experimental analysis. Noise in electronic systems is often characterized by its Power Spectral Density (PSD), which describes how the power of a signal is distributed across different frequency components. The PSD is defined as the Fourier transform of the autocorrelation function:

$$P_{XX}(f) = \sum_{m=-\infty}^{\infty} r_{xx}(m) e^{-j2\pi fm}, \tag{4.3}$$

and provides information about the autocorrelation structure of the signal. The strength of the Fourier transform in signal analysis lies in its ability to reveal spectral structures that can be used to characterize a signal (53).

Several methods have been developed for PSD estimation, categorized into non-parametric and parametric approaches. Parametric methods assume that the signal follows a specific statistical model and estimate the PSD by fitting parameters to this model. Common techniques include the autoregressive (AR) model (54), the moving average (MA) model, and the autoregressive-moving-average (ARMA) model (55). These methods often provide high spectral resolution, however require careful selection of model parameters, making them sensitive to estimation errors (56).

Non-parametric methods, on the other hand, do not assume an underlying model and estimate the PSD directly from the Fourier transform of the signal. The periodogram is the most basic approach, computing the squared magnitude of the discrete Fourier transform (DFT), but it suffers from high variance and spectral leakage (57). The Bartlett method improves upon this by averaging periodograms from non-overlapping segments, reducing variance at the cost of frequency resolution (58). In 1967, Welch introduced an extension of Bartlett's approach, reducing variance by using overlapping segments and applying a window function before computing the periodograms (59). These techniques remain widely used due to their simplicity and computational efficiency (60).

In this work, Welch's method was chosen for PSD estimation of electronic noise due to its robustness and widespread acceptance in the literature. Additionally, the averaging of overlapping segment spectra reduces the statistical variance of the estimate, while windowing mitigates spectral leakage, making it a reliable choice for analyzing random signals such as electronic noise ((54), (60)) . Furthermore, its efficient implementation, available in scientific libraries such as *scipy.signal.welch* (61), facilitates practical application.

Knowing the PSD of the noise, the temporal noise $n(t)$ can be obtained by defining a phase spectrum. Thus, after estimating the Average Power Spectral Density of the real noise dataset via the Welch method, the noise generation will follow the steps outlined below (62):

1. Recreate the spectrum for "negative" frequencies, since the PSD is only represented for positive frequencies.
2. Introduce a phase spectrum $\phi(f)$ as a random process with a uniform distribution

between $-\pi$ and $+\pi$:

$$f > 0 \rightarrow N(f) = \sqrt{\frac{PSD(f)}{2}} \times e^{j\phi f} \tag{4.4}$$

$$f < 0 \rightarrow N(f) = \sqrt{\frac{PSD(f)}{2}} \times e^{-j\phi f} \tag{4.5}$$

$$f = 0 \rightarrow N(0) = DC \tag{4.6}$$

3. Perform an IFFT to obtain the time-domain noise series:

$$n(t) = \text{Re}\{\text{IFT}[N(f)]\} \tag{4.7}$$

The method for noise generation, as described above, will be employed in the Chapter 5, where it will be used to simulate the electronic noise present in the PMT signals based on the estimated Power Spectral Density.

4.3.2 Output signal

In Section 4.1, the proposed simulation algorithm was described. As highlighted, the output signal will consist of a waveform formed by the SPE signals combined with electronic noise. The shape and temporal behavior of this signal will be solely determined by the photon arrival times following the photon propagation stage.

In the experiment, Fast and Slow Digitizers collect and digitize the PMT signals. Consequently, the simulation must incorporate the digitization process, including waveform quantization based on the Analog-to-digital Converter (ADC) resolution of the digitizers.

As shown in Table 3, both digitizers have a 12-bit resolution. Therefore, the ADC voltage resolution can be calculated as follows:

$$ADC\_Voltage_{Resolution} = \frac{V_{range}}{2^{bits} - 1} \tag{4.8}$$

$$ADC\_Voltage_{Resolution} = \frac{1\ V}{2^{12} - 1} = 0.244\ mV \tag{4.9}$$

This stage is crucial, as it scales the signal within the digitizers' range and discretizes the waveform amplitudes.

Figure 21 illustrates the fluxogram of the output signal generation process.

Figure 21 – Fluxogram of the output signal generation process.

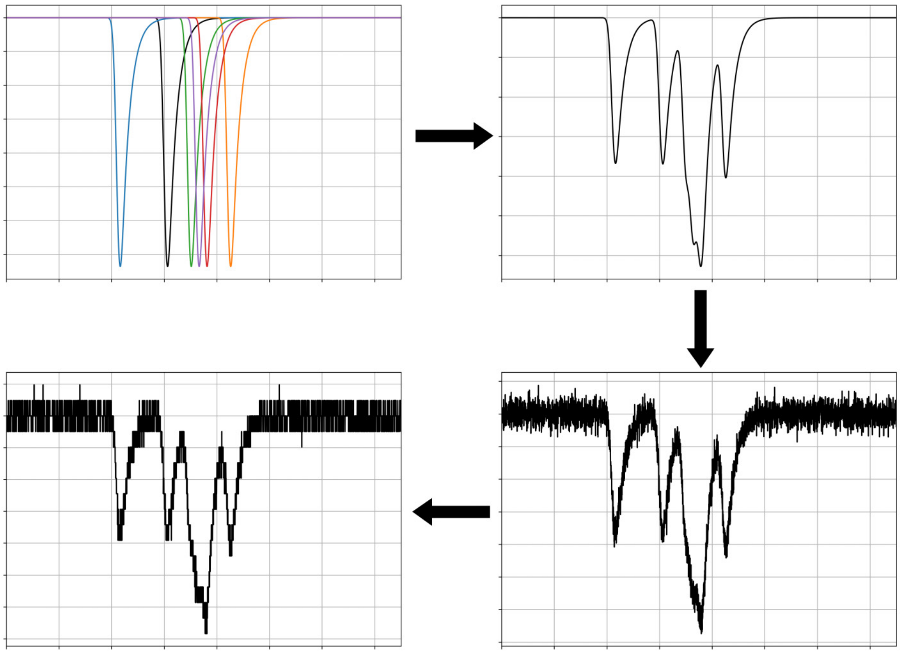

Source: Prepared by the author (2024).

5 PMT CHARACTERIZATION

This chapter covers the entire PMT characterization process. The first section is focused on the characterization of the Single Photoelectron (SPE) Signal. Next, the PMT gain characterization is addressed. Finally, the electronic noise characterization is presented.

5.1 SINGLE PHOTOELECTRON SIGNAL

As mentioned in the previous sections, the single photoelectron signal is the main element of the simulation. Its characterization was divided into the following steps: data acquisition, signal analysis, and obtaining the optimal parameters for the SPE signal model. The details will be shown in the following subsections.

5.1.1 Data acquisition setup

The setup used to acquire SPE signal data consists of the Hamamatsu PMT R7378A, operated at a supply voltage of 900 V, and a light pulse generator (LPG). The Tedeldyne Lecroy WaveSurfer 4104HD oscilloscope (63) was used to realize the measurements. Its most relevant technical specifications for our analysis are shown in Table 5. For more details on the data acquisition procedure and setup, see (51).

Table 5 – WS4104HD Specifications

Specification	Description
Analog Bandwidth (Max)	1 GHz
Analog Sample Rate	5 GS/s
Analog Vertical Resolution	12 bits

Source: WaveSurfer 4000HD High Definition Oscilloscopes (200 MHz - 1 GHz) Datasheet.

5.1.2 SPE signal dataset

The SPE signal dataset consists of 1000 waveforms, each with 1002 samples in a 200 ns time window. Due to the quantum efficiency of the PMT, the dataset contains both SPE signals and noise-only signals. Figure 22 illustrates both cases.

As shown in the examples, the database contains very noisy waveforms, which makes the characterization of the SPE signal more difficult.

Figure 22 – Examples of SPE dataset signals. On the left, a noise-only signal. On the right, a SPE signal.

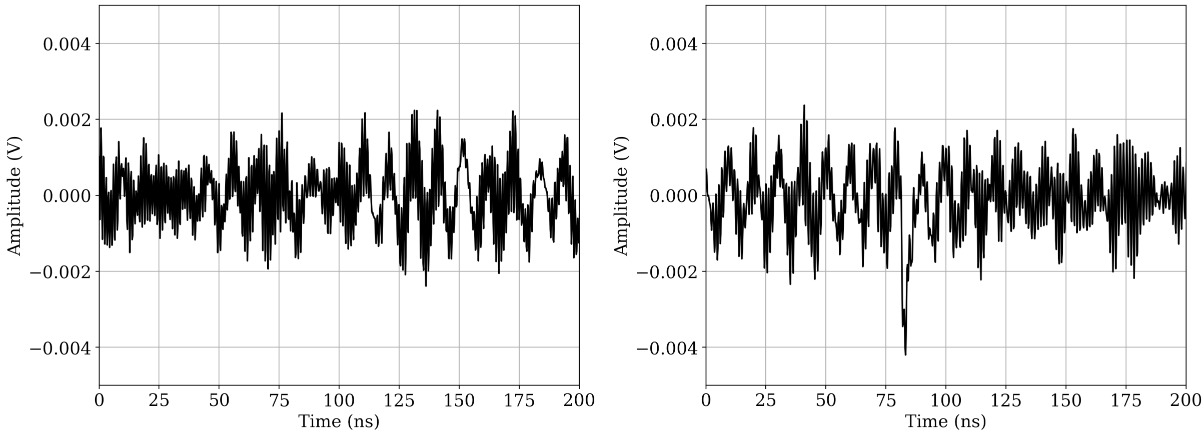

Source: Prepared by the author (2024).

5.1.3 SPE signal shape

The anode circuit of the PMT can be represented by a Norton Equivalent Circuit (64), as shown in Figure 23.

Figure 23 – PMT anode equivalent circuit

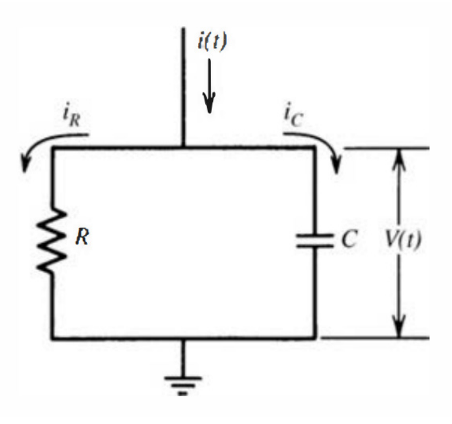

Source: Extracted from (64)

Given that the output circuit is a typical RC circuit, an exponential decay is expected during the signal's fall. In the literature, various models have been employed to represent the shape of the SPE pulse response, including combinations such as Exponential + Gaussian (65), Lognormal ((66), (67)), and Gaussian (68), offering flexibility to adapt to different experimental conditions and detector responses.

Therefore, to capture the signal's asymmetry caused by the exponential decay, the shape of an Exponentially Modified Gaussian, already described in Section **4.2.2**, was opted to model the SPE signal. Given that its PDF has a unit area, modeling the SPE signal involves scaling the PDF by the total signal area.

To calculate the total charge of a signal, we simply used the definition of electric current,

$$i(t) = \frac{v(t)}{R} = \frac{dQ}{dt} \tag{5.1}$$

The total charge of the signal is given by the integral of the waveform amplitude over its duration, divided by the terminal resistance, as follows,

$$Q = \frac{1}{R}\int_{t_0}^{t_1} v(t)\, dt \tag{5.2}$$

Thus, the total signal area is:

$$\int_{t_0}^{t_1} v(t)\, dt = Q \cdot R \tag{5.3}$$

Finally, the shape model of the SPE signal can be defined as:

$$v(t)_{SPE} = Q \cdot R \cdot \frac{\lambda}{2} \exp\left(\frac{\lambda}{2}(2\mu + \lambda\sigma^2 - 2t)\right) \operatorname{erfc}\left(\frac{\mu + \lambda\sigma^2 - t}{\sqrt{2}\sigma}\right) \tag{5.4}$$

Additionally, the total charge of the PMT output signal can also be calculated as follows,

$$Q = G \cdot N \cdot (-e), \tag{5.5}$$

where:

- G is the gain of the PMT.
- N is the number of photoelectrons at the cathode, thus $N = 1$.
- e is the elementary charge, thus $e = 1.6 \times 10^{-19}\,\mathrm{C}$.

Therefore, the Equation 5.4 can be rewritten as follows.

$$v(t)_{SPE} = -\ G \cdot e \cdot R \cdot \frac{\lambda}{2} \exp\left(\frac{\lambda}{2}(2\mu + \lambda\sigma^2 - 2t)\right) \operatorname{erfc}\left(\frac{\mu + \lambda\sigma^2 - t}{\sqrt{2}\sigma}\right) \tag{5.6}$$

Both Equations (5.4) and (5.6) define the SPE signal shape. However, the former was chosen for the next subsection to fit the single photoelectron signals and estimate the charge, along with the parameters σ and λ.

5.1.4 SPE signal characterization

As mentioned in Section **5.1.2**, the dataset contains both noise and SPE signals. To eliminate part of the noise signals, an initial analysis of the peak amplitude positions is performed.

Figure 24 – Peak amplitude position histogram

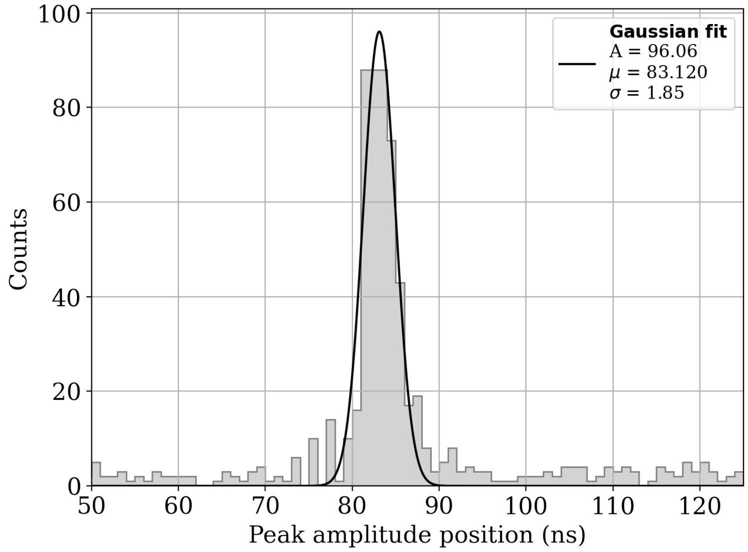

Source: Prepared by the author (2024).

Through a visual analysis of the histogram, shown in Figure 24, and its Gaussian fit, it is concluded that the SPE signals are predominantly distributed within $\pm 3\sigma$ around the mean of the fit. Signals outside this range are composed predominantly of noise. Based on this, a cut in this range was applied to the data, reducing the number of waveforms from 1000 to 444.

The characterization procedure follows four steps:

1. Selection of a time window of interest: Where the SPE signal occurs.
2. Fit of noise and SPE signal: For the noise, is used sine functions. For the SPE signal, the Equation (5.4) is used.
3. Noise removal from the fit described in Step 2.
4. Estimation of the SPE signal shape.

An example of the procedure is shown in Figure 25. The same is done for the entire dataset.

Figure 25 – SPE signal characterization example

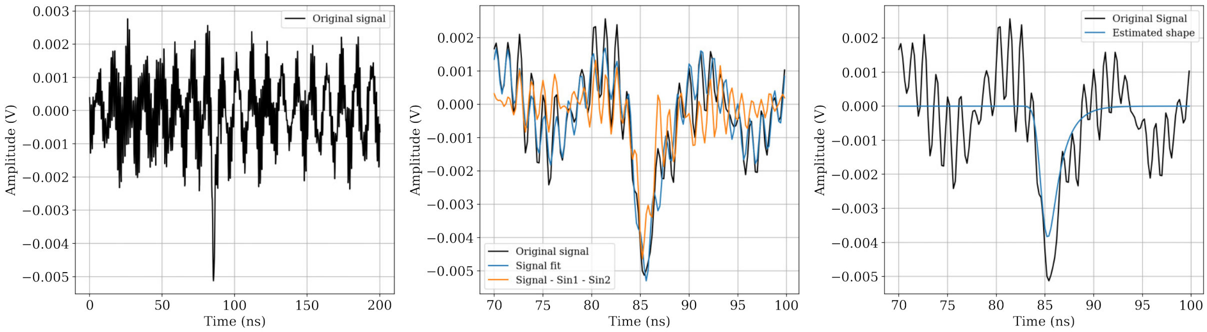

Source: Prepared by the author (2024).

After performing the procedure for the entire dataset, the histograms for charge, σ and λ are obtained. To obtain the best parameters, a Gaussian fit was imposed on the histograms. The results are shown in Figures 26, 27, and 28.

Figure 26 – Charge distribution histogram

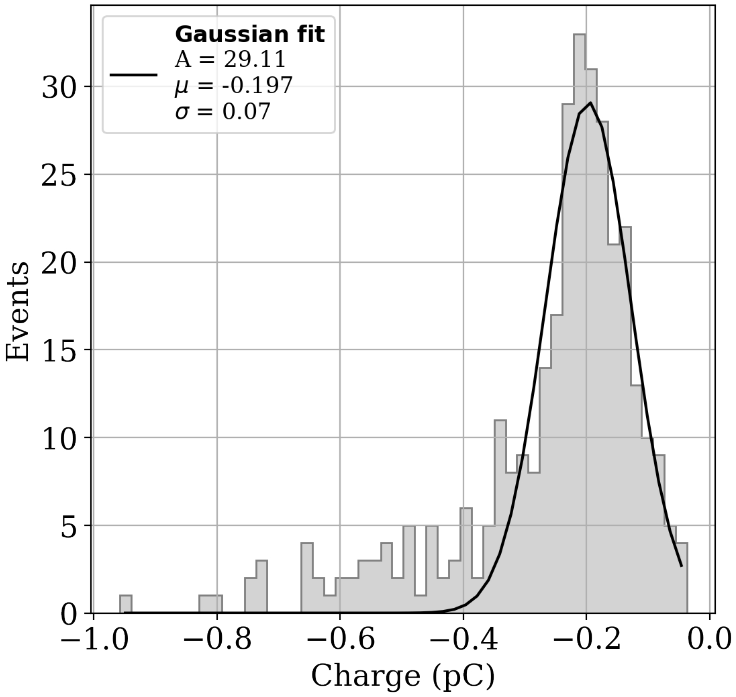

Source: Prepared by the author (2024).

As we obtained the charge of the SPE signal through the histogram, we can then calculate the PMT gain using Equation 5.5, as follows:

Figure 27 – σ distribution histogram

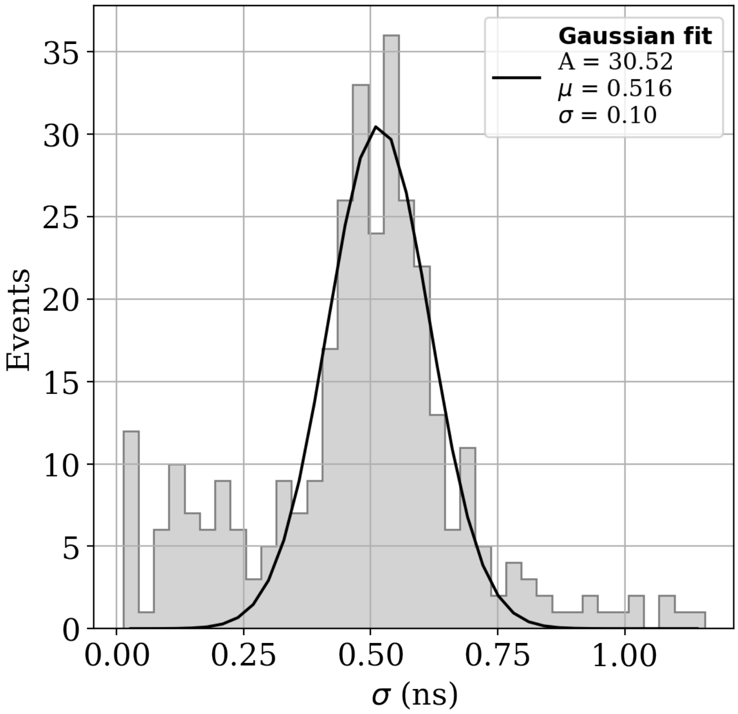

Source: Prepared by the author (2024).

$$-0.197 \times 10^{-12} = G \cdot 1 \cdot (-1.6 \times 10^{-19})$$

$$G = 1.23 \times 10^{6}$$

It is important to note that this result corresponds to the PMT operating at a supply voltage of 900V.

Finally, the SPE signal model found for the PMT R7378A is shown in Figure 29.

The final results of the obtained parameters for the SPE signal characterization are summarized in Table 6. These results are reasonable when compared with the values described in the PMT datasheet (45). For the gain, the typical value for a supply voltage of 900 V is 0.9×10^{6}, as presented in Figure 11. The value found through characterization, however, was 1.23×10^{6}, indicating a deviation that can be attributed to variations in individual PMT responses or slight differences in the experimental setup.

Regarding the rise time, the typical value is 1.5 ns, as described in Table 1, while the calculated value was 1 ns. This discrepancy could be related to the specific configuration of the signal acquisition system, which may affect the observed signal shape.

Figure 28 – λ distribution histogram

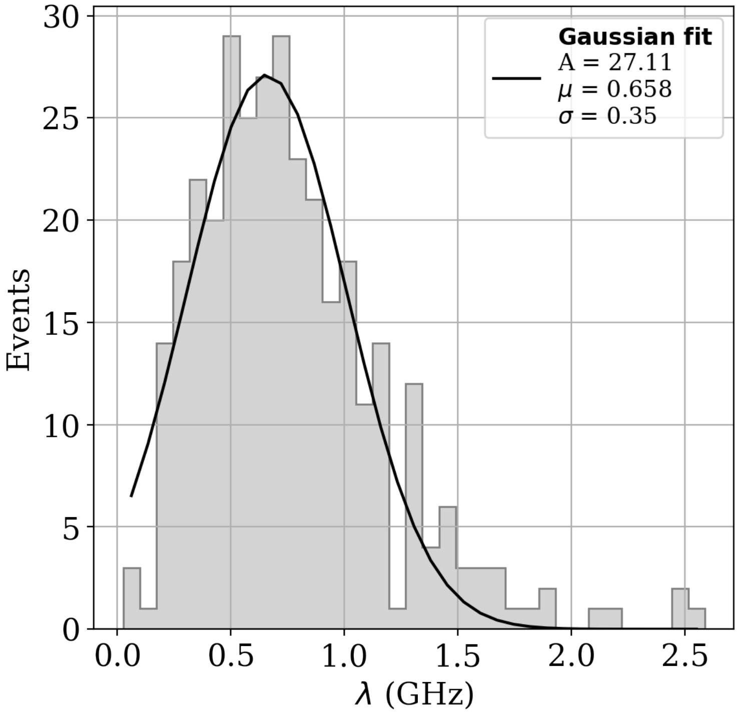

Source: Prepared by the author (2024).

Figure 29 – SPE signal model for a supply voltage of 900 V

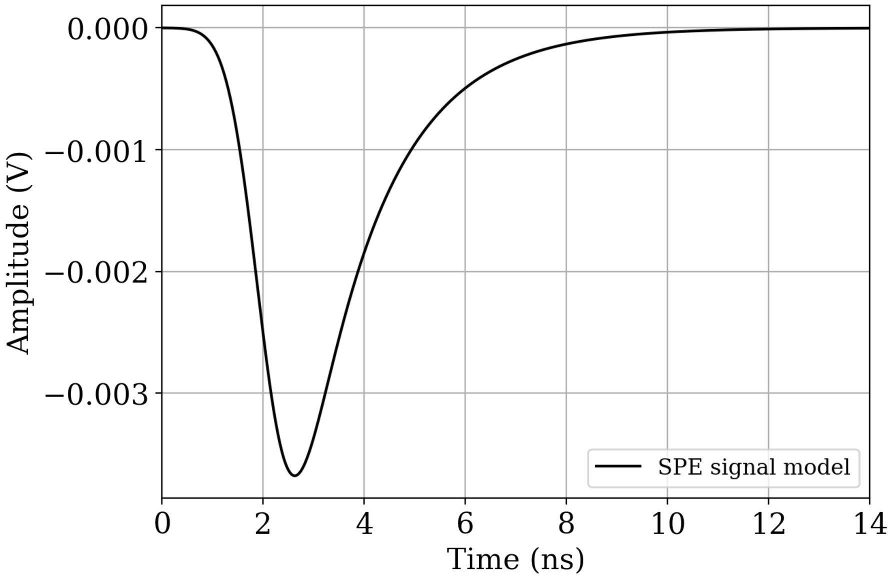

Source: Prepared by the author (2024).

Table 6 – SPE signal model parameters for PMT operating at 900 V

Parameters	**Value**
PMT Gain	1.23×10^6
Charge (pC)	-0.197 ± 0.070
σ (ns)	0.516 ± 0.100
λ (GHz)	0.658 ± 0.350
Rise time (ns)	1
Fall time (ns)	3.4
FWHM (ns)	2.2

Source: Prepared by the author (2024).

5.2 PMT GAIN

In Section 5.1, the SPE signal function was defined, along with its model for a PMT supply voltage of 900 V. However, as mentioned in Section **3.2.2**, the PMTs in the experimental setup are calibrated at different voltages.

Therefore, the gain of the PMT R7378A will be characterized to determine the gain curve as a function of the supply voltage by the end of this section.

5.2.1 Dataset with higher intensity of light

In addition to the SPE dataset, datasets for a fixed intensity of a LPG were also acquired. Five acquisitions were made, each with a different supply voltage level and 1000 waveforms.

Figure 30 displays the average waveform for each level of supply voltage.

Figure 30 – Average waveform for each supply voltage level

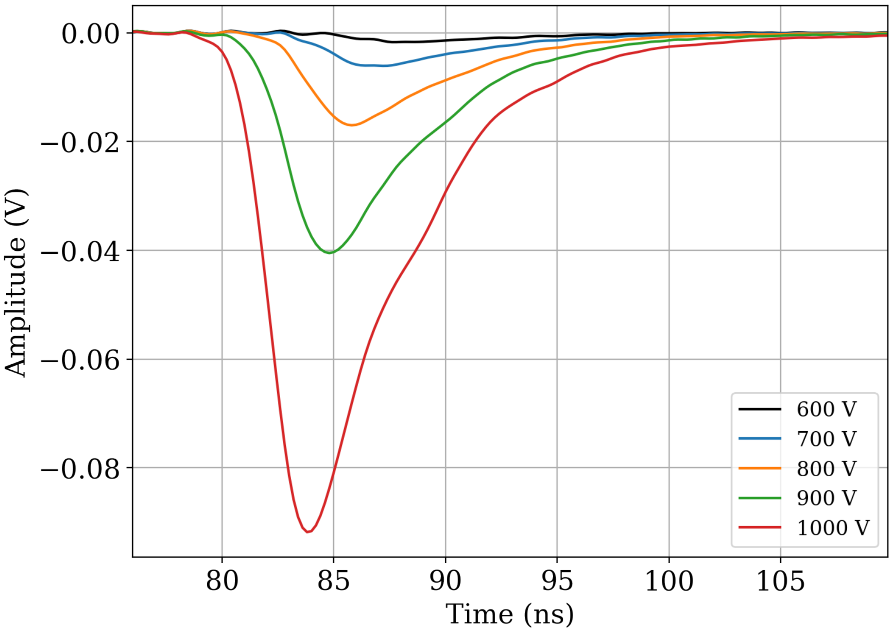

Source: Prepared by the author (2024).

5.2.2 Gain characterization

As the SPE signal was characterized in Section **5.1.4** for a supply voltage of 900 V, it is possible to estimate the average number of emitted photoelectrons in the average waveforms from Figure 30.

Since the PMT R7378A datasheet does not provide any information regarding its collection efficiency, we will consider it to be 100% for all supply voltage levels.

To calculate the average number of released photoelectrons, Equation (5.4) is applied to compute the charge of the average waveform at 900 V, which is then divided by the charge of the SPE signal, as follows,

$$Q = \frac{1}{R}\int_{t_0}^{t_1} v_{900V}(t)\,dt = -6.0\ pC$$

$$N_{pe} = \frac{Q}{Q_{spe}} = \frac{-6.0\ pC}{-0.197\ pC} \approx 30$$

With this number estimated, the PMT gain for the remaining supply voltage levels can be determined. For that, the charge of each average waveform is calculated using Equation (5.2), and by substituting it into Equation (5.5) along with the estimated number of photoelectrons, the gain is obtained. The results of this procedure are presented in Table 7.

Table 7 – PMT gain for different supply voltage levels

Supply Voltage	**Avg. waveform charge**	**SPE signal charge**	**Gain**
600 V	$-0.274\ pC$	$-0.009\ pC$	0.056×10^6
700 V	$-0.982\ pC$	$-0.032\ pC$	0.201×10^6
800 V	$-2.560\ pC$	$-0.084\ pC$	0.525×10^6
900 V	$-6.000\ pC$	$-0.197\ pC$	1.230×10^6
1000 V	$-13.140\ pC$	$-0.431\ pC$	2.697×10^6

Source: Prepared by the author (2024).

After determining the gain values for each voltage level, it is now possible to obtain the gain curve as a function of the supply voltage. The gain of a PMT can also be determined using the following equation (42):

$$G = A \cdot V^{k \cdot n}, \tag{5.7}$$

where:

- V is the supply voltage.
- A is a constant.
- k is determined by the structure and material of the dynode and has a value from 0.7 to 0.8.
- n is the number of dynodes stages. For PMT R7378A, $n = 10$ (45).

For this purpose, Equation 5.7 will be applied to fit the data points from Table 7, which were previously calculated. Figure 31 shows the resulting curve along with the optimal fit parameters.

Figure 31 – Gain in function of the supply voltage

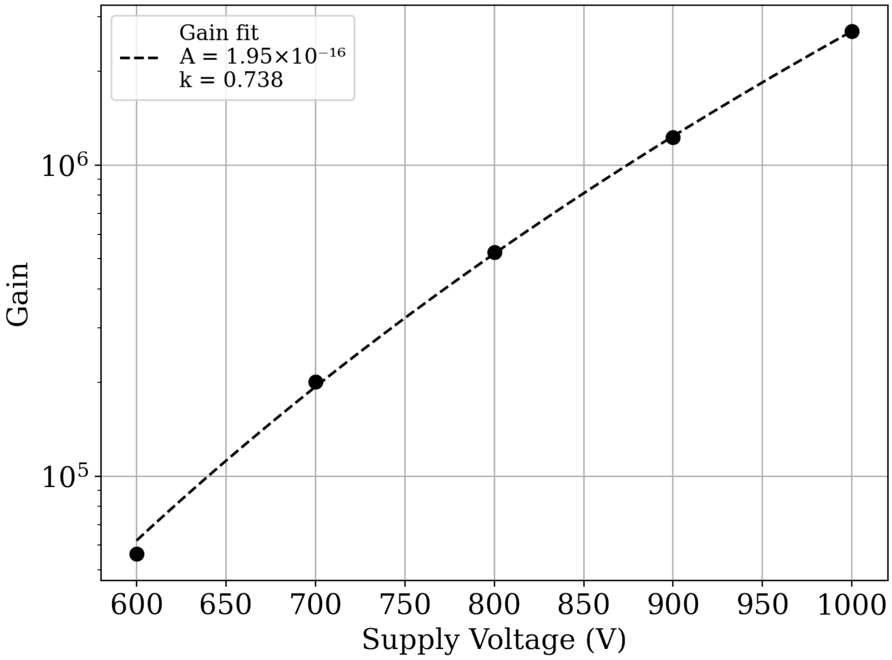

Source: Prepared by the author (2024).

As listed in Table 2, the PMTs in the LIME setup are calibrated with different supply voltages. For the PMT characterized in this section, the supply voltage to be considered is 772 V. Thus, the calibrated PMT gain is obtained using the Equation (5.7) with the optimal fit parameters from Figure 31, as follows:

$$G_{772V} = 1.95 \times 10^{-16} \cdot 772^{0.738 \cdot 10} = 0.398 \times 10^{6} \tag{5.8}$$

Finally, after determining the calibrated gain, the SPE signal is obtained using Equation (5.6), as illustrated in Figure 32.

Therefore, all the necessary parameters for the simulation related to the SPE signal have been calculated and adjusted according to the calibration of the experimental setup.

5.3 ELECTRONIC NOISE

In this section, the used noise dataset will be described, as well as its characterization. Finally, a comparison will be made between the real noise dataset and the simulated noise dataset.

Figure 32 – SPE signal for a supply voltage of 772 V

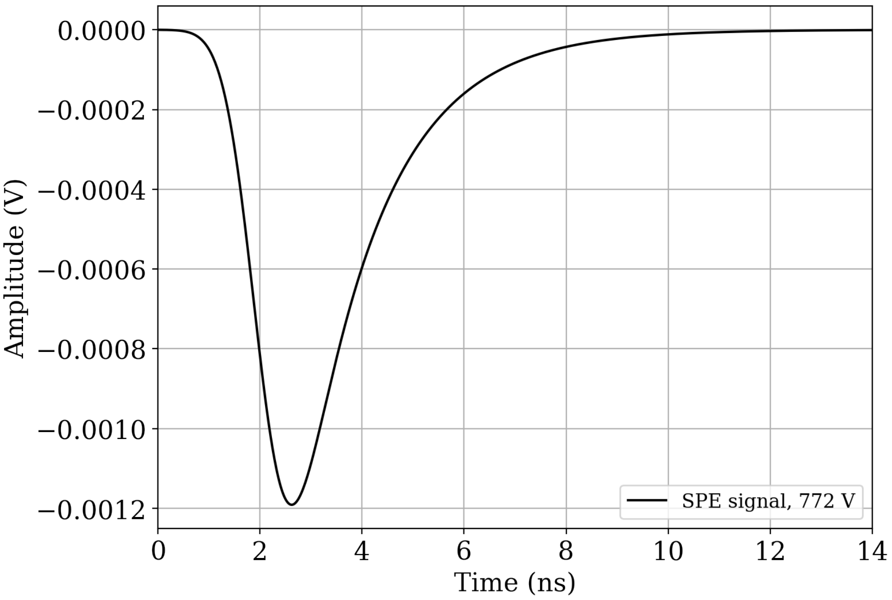

Source: Prepared by the author (2024).

5.3.1 Noise dataset

The experimental setup includes two digitizers to collect the waveforms generated by the four PMTs. Therefore, it is necessary to characterize the noise for each digitizer channel, resulting in a total of eight noise characterizations.

For each channel, a real noise dataset containing 1,000 waveforms was selected. Figure 33 and 34 show examples of noise waveforms for the Fast and Slow digitizers, respectively.

5.3.2 Noise characterization

Using the real dataset available for each channel, the noise characterization is performed following the procedure outlined in Section **4.3.1**. For each channel, the PSD is computed for all 1,000 waveforms in the dataset. Finally, the average PSD is obtained. The resulting PSDs for each digitizer are shown in Figure 35.

A visual analysis of Figure 35 reveals that the noise characteristics of the channels are not identical, highlighting the importance of individual characterization.

After obtaining the average PSDs, a dataset of 1,000 simulated noise signals was generated for each PMT to match the size of the real noise dataset. Figures 36 and 37 present a comparison of the PSDs of the simulated and real noise signals, for the Fast and Slow digitizers. Similarly, Figures 38 and 39 show histograms comparing the amplitude distributions.

Figure 33 – Examples of noise waveforms for the Fast digitizer (reduced time window)

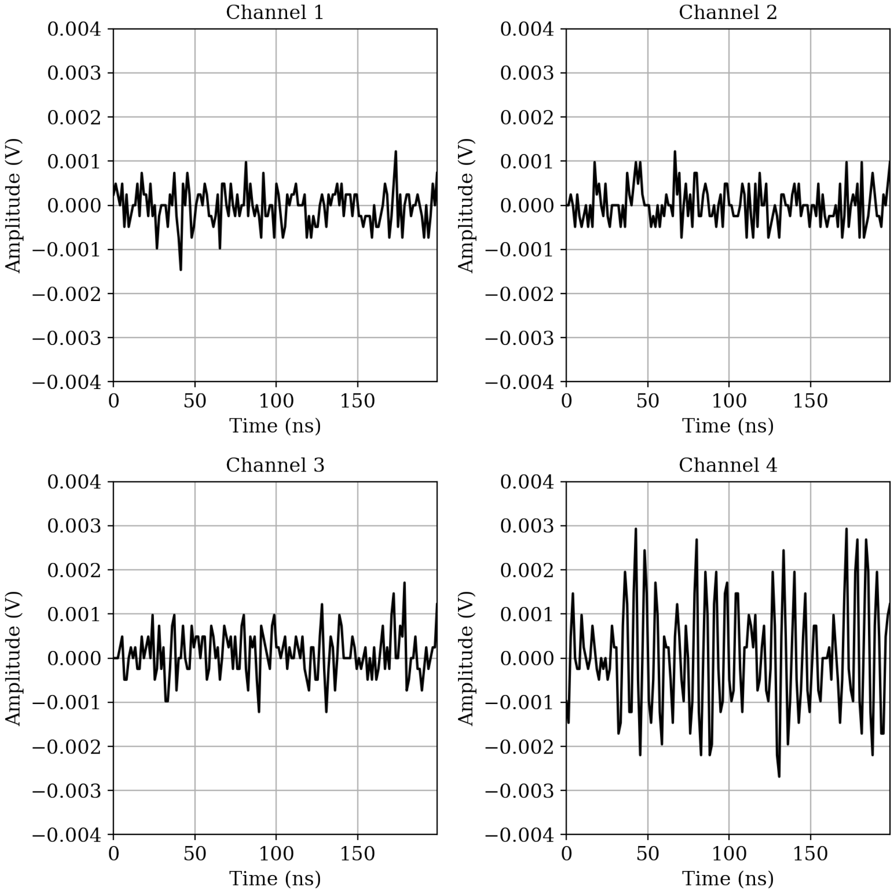

Source: Prepared by the author (2024).

The discretization of the amplitude histograms results from the quantization of the signals, reflecting the resolution of the digitizers. Additionally, the PSDs of simulated and real noise show a significant overlap, as do the amplitude histograms, validating the noise generation method employed in this work.

Figure 34 – Examples of noise waveforms for the Slow digitizer (reduced time window)

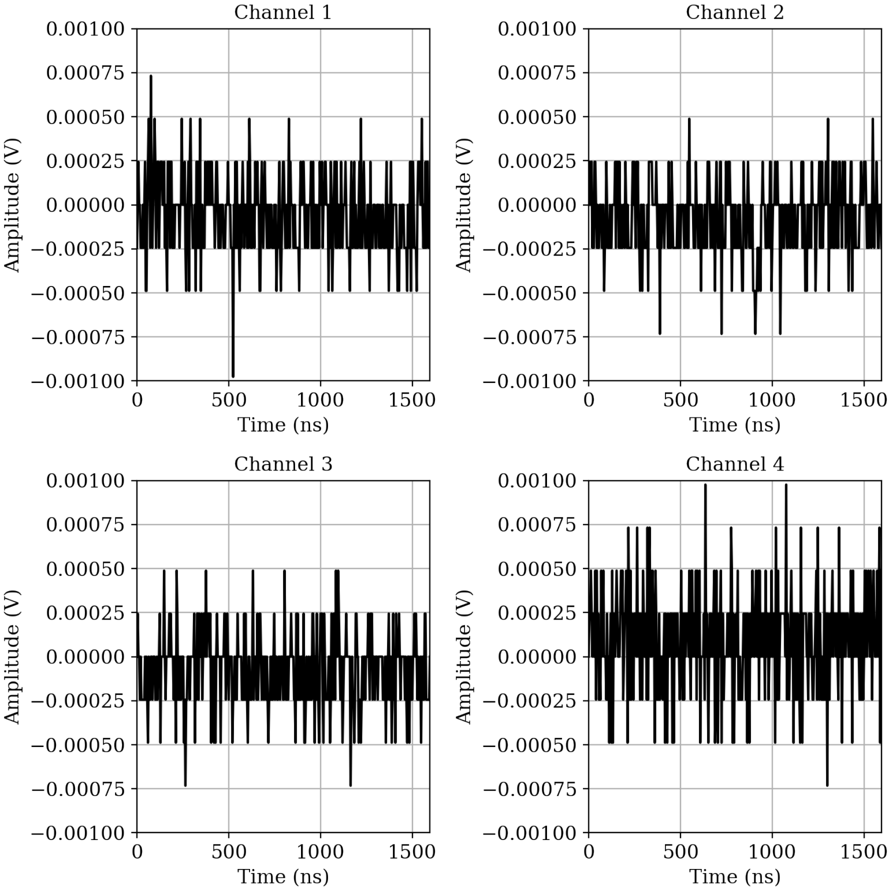

Source: Prepared by the author (2024).

Figure 35 – Average PSDs of real noise dataset. On the left, for the Fast digitizer. On the right, for the Slow digitizer

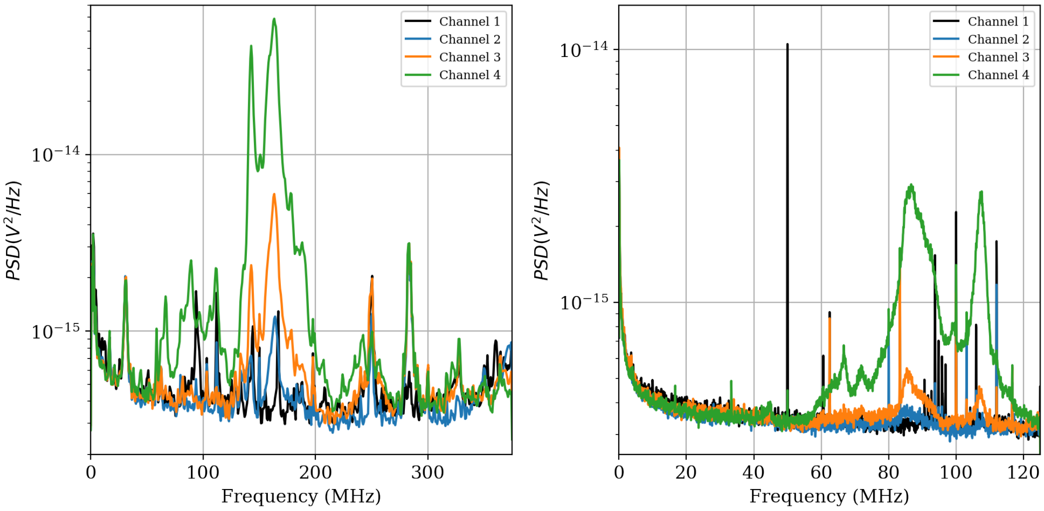

Source: Prepared by the author (2024).

Figure 36 – Average PSD of real and simulated noise for the Fast digitizer

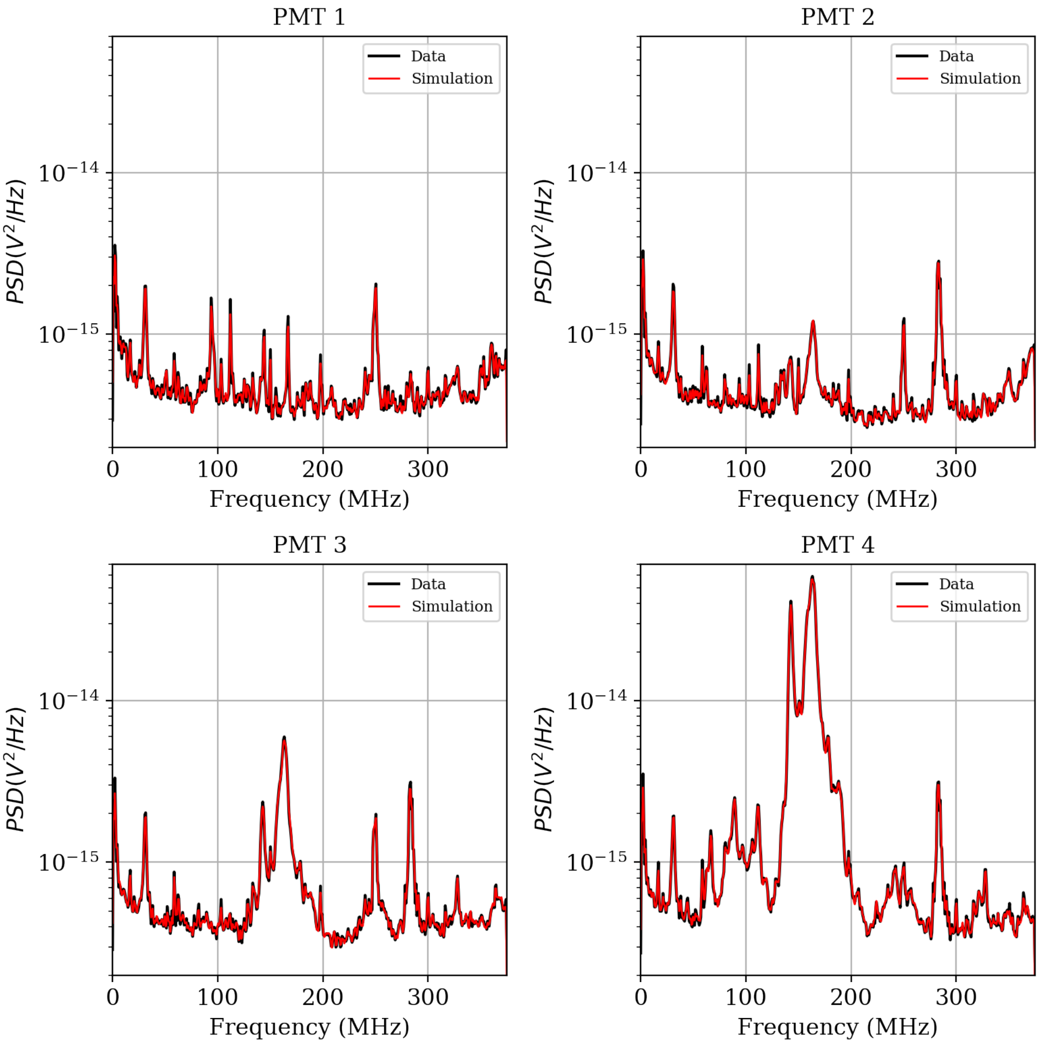

Source: Prepared by the author (2024).

Figure 37 – Average PSD of real and simulated noise for the Slow digitizer

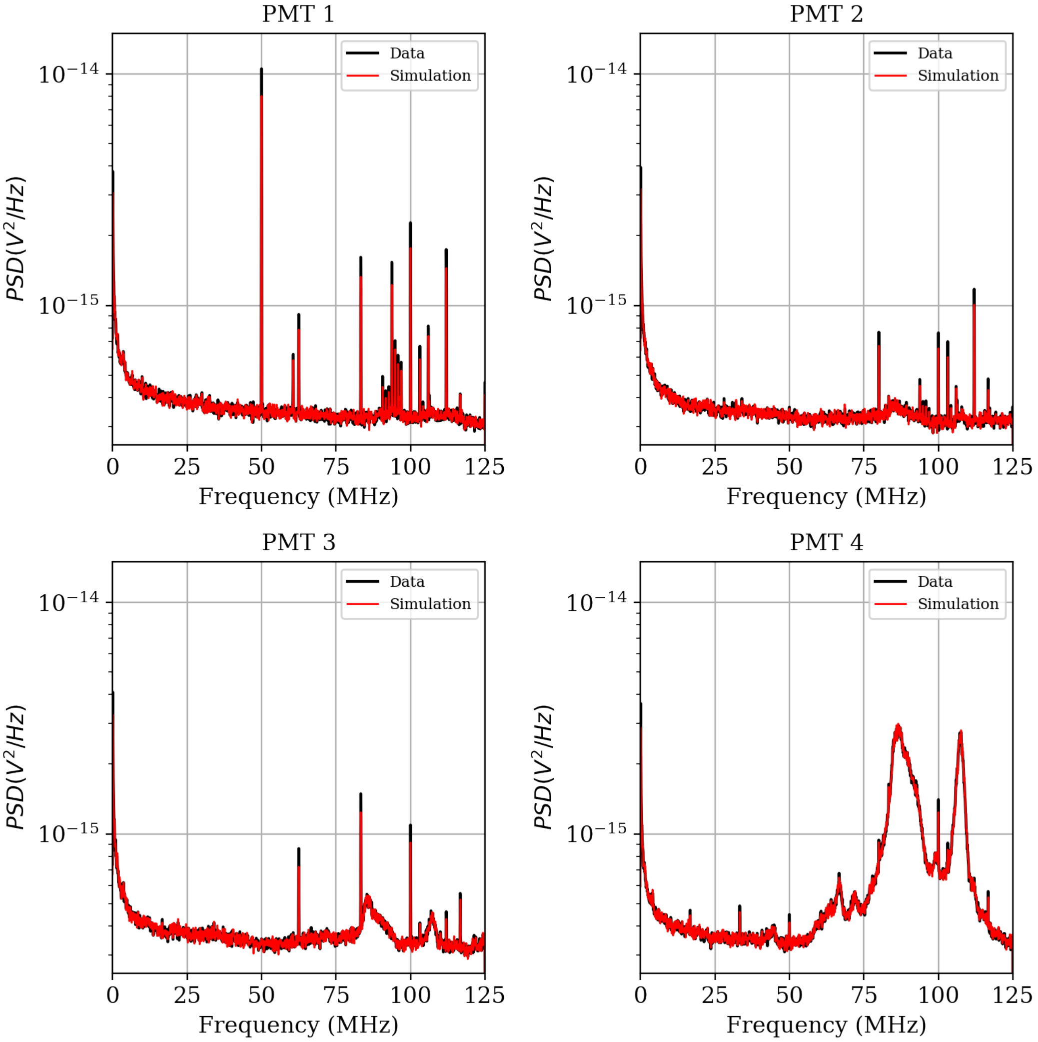

Source: Prepared by the author (2024).

Figure 38 – Amplitude distribution of real and simulated noise for the Fast digitizer

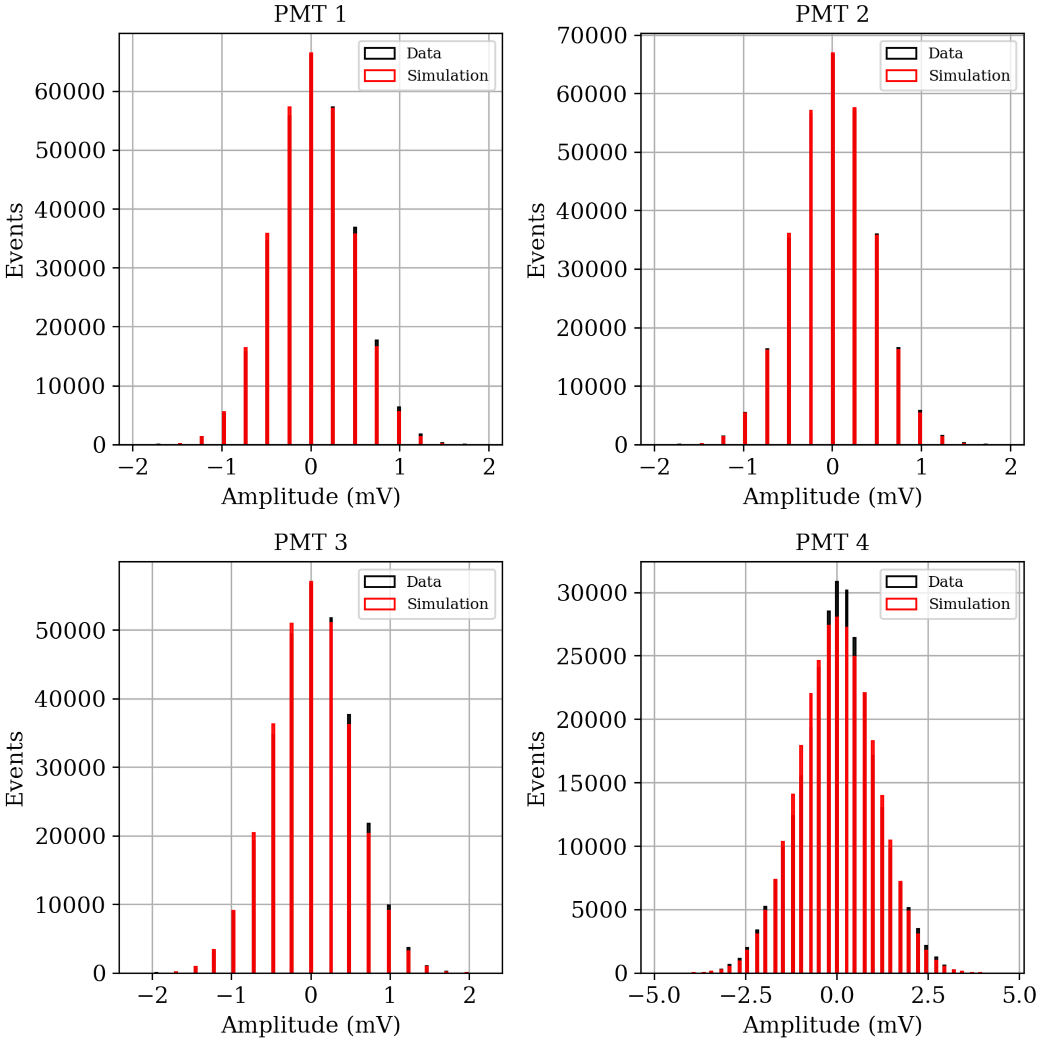

Source: Prepared by the author (2024).

Figure 39 – Amplitude distribution of real and simulated noise for the Slow digitizer

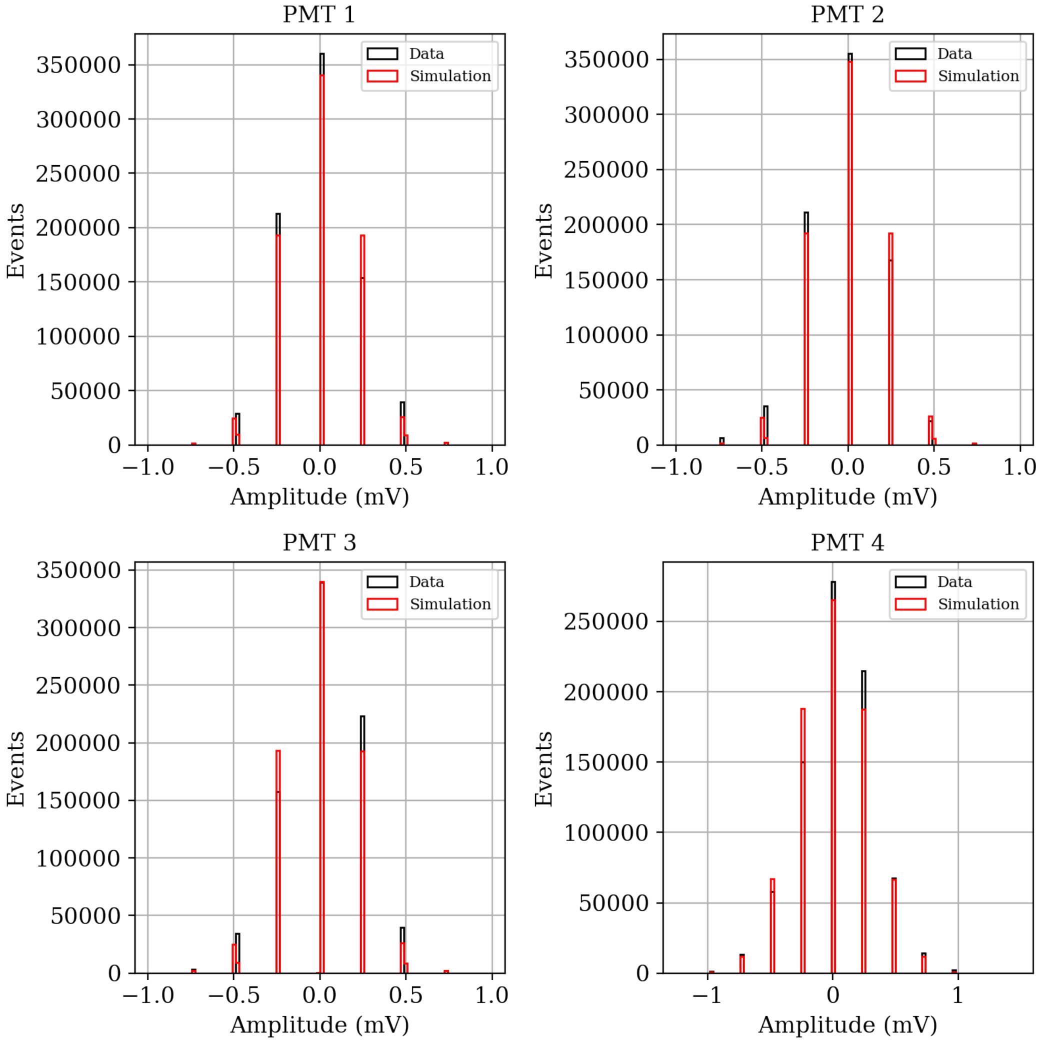

Source: Prepared by the author (2024).

6 RESULTS

In this chapter, simulation examples will be presented, combining the LIME detector simulation software with the PMT simulation software developed throughout this work. Finally, a comparative analysis with experimental data will be performed.

6.1 SIMULATION EXAMPLES

Since the ^{55}Fe events are quite typical, their simulation is straightforward. In this case, to simulate an image containing these events, 6 keV energy spots are simulated, and the x-y positions on the GEM plane, as well as the z position, are defined in the configurations of the LIME detector simulation software.

As mentioned in Section **3.2.2**, the use of two digitizers allows for the capture of signals with both short and long time extensions. However, typical signals from ^{55}Fe events are very fast and, consequently, are better visualized with the Fast digitizer rather than the Slow digitizer. For this reason, the waveforms from the Slow digitizer will be displayed in the same time window as the Fast digitizer.

The first two examples to be demonstrated are when the ^{55}Fe spot is centered, at the positions z = 50 mm and z = 466 mm, respectively. In this situation, the distance from the spot to each of the PMTs is the same, so the simulated PMT signals should be similar, as can be seen in Figures 40 and 41.

The third and fourth examples demonstrate the situation when the ^{55}Fe spot is positioned at the x-y coordinates of one of the PMTs, at the z positions of 50 mm and 466 mm, respectively. In this case, the spot is closer to that PMT, at an intermediate distance from the adjacent PMTs, and farther from the opposite PMT. Therefore, the simulated PMT signals should exhibit behavior consistent with this situation, as shown in Figures 42 and 43.

Simulations for different z positions are important as they allow for the visualization and analysis of the temporal behavior of the waveforms due to z diffusion. As the z distance increases, the diffusion becomes more significant, leading to an increase in the signal width.

Additionally, simulating different x-y positions of the ^{55}Fe spot enables the evaluation of the dependence on the R distance through the signal amplitudes. This analysis helps characterize how the proximity of the event to each PMT influences the generated signals.

6.2 COMPARATIVE ANALYSIS WITH EXPERIMENTAL DATA

To evaluate the performance of the developed simulation, we will conduct a more in-depth comparison, taking into account the x-y-z positions of the events occurring in the detector. For this comparison, ^{55}Fe runs from the Daily Calibration will be used.

This analysis will be based on the following steps:

1. Take the x-y-z position of the ^{55}Fe spots in the image.
2. Associate the spots with the PMTs waveforms.
3. Perform a waveform analysis to get valuable information.
4. Evaluate the information from the waveform analysis in function of the R distance between the ^{55}Fe spot at the GEM and the PMTs.

These steps will be applied to the real data. For the simulated data, only the first step will be modified. Instead of extracting the x-y-z positions from real images, events will be simulated at various x-y positions on the GEM and across the z-values from Daily Calibration to assess the effects of diffusion.

In the waveform analysis step, the following parameters will be evaluated:

- Peak amplitude.
- Charge, using the Equation 5.2.
- RMS_{noise}, calculated as follows,

$$RMS_{noise} = std(v_{noise}(t)) \tag{6.1}$$

- Signal-to-noise Ratio (SNR), calculated as follows,

$$SNR = \frac{Peak}{RMS_{noise}} \tag{6.2}$$

- Full Width at Half Maximum
- Full Width at the Baseline

The comparative analysis is performed by scanning five different positions along the z-direction, identical to the positions used in the ^{55}Fe Daily Calibration runs (see Section **3.2.3**). Additionally, the results will be displayed as a function of the R distance, which can be calculated as:

$$R = \sqrt{(X_{\text{PMT}} - x_0)^2 + (Y_{\text{PMT}} - y_0)^2 + (Z_{\text{PMT}} - z_0)^2}, \tag{6.3}$$

where:

- x_0 e y_0 are the x-y position of the ^{55}Fe spot in the image.

- $z_0 = 0$ is the GEM plane.

Figure 44 shows the results for the ^{55}Fe source positioned at z = 50 mm (Step 1). The results for the other z positions can be found in Appendix A. Recalling the information presented in Section **4.2.1**, the results were obtained using $\alpha = 3.65$ in the relationship $1/R^{\alpha}$.

An analysis of the results from the obtained figures reveals that the FWHM and Full Width at the Baseline measurements are independent of the x and y positions, depending solely on the z position. Consequently, it is possible to plot these two parameters as a function of the z distance from the GEM plane, as presented in Figure 45.

It is evident that the simulation data shows a high degree of agreement with the experimental data for most parameters. However, two exceptions stand out: the FWHM and Full Width at the Baseline, which exhibit a significant discrepancy, mainly for the Steps 1, 2 and 3. Since these parameters are related to the temporal spread of the signal, the observed difference might be due to temporal dispersion effects.

As previously discussed in Section **4.2.2**, after excluding the known dispersions, the missing temporal dispersion component in the photon propagation was characterized using an exponential distribution. However, this leads to the question of whether this missing component could have a different PDF than the exponential one. Since the EMG already accounts for the Gaussian dispersions in the system, it is possible that part of these Gaussian dispersions is not fully captured in the model. If that's the case, this overlooked Gaussian dispersion might be influencing the temporal spread in a way that reduces the spread of the exponential component. As a result, the new PDF could imply that a larger portion of the photons experiences Gaussian dispersion, leading to a more concentrated temporal distribution, rather than a wider one. Therefore, further investigations into the exact nature of the temporal dispersion and its impact on the measurements would be necessary to better understand the observed discrepancies.

Figure 40 – Simulation example 1: Centered ^{55}Fe spot, z position = 50 mm

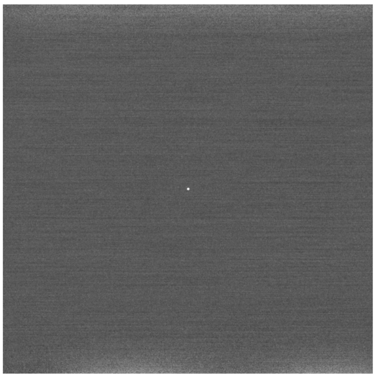

(a) Simulated image.

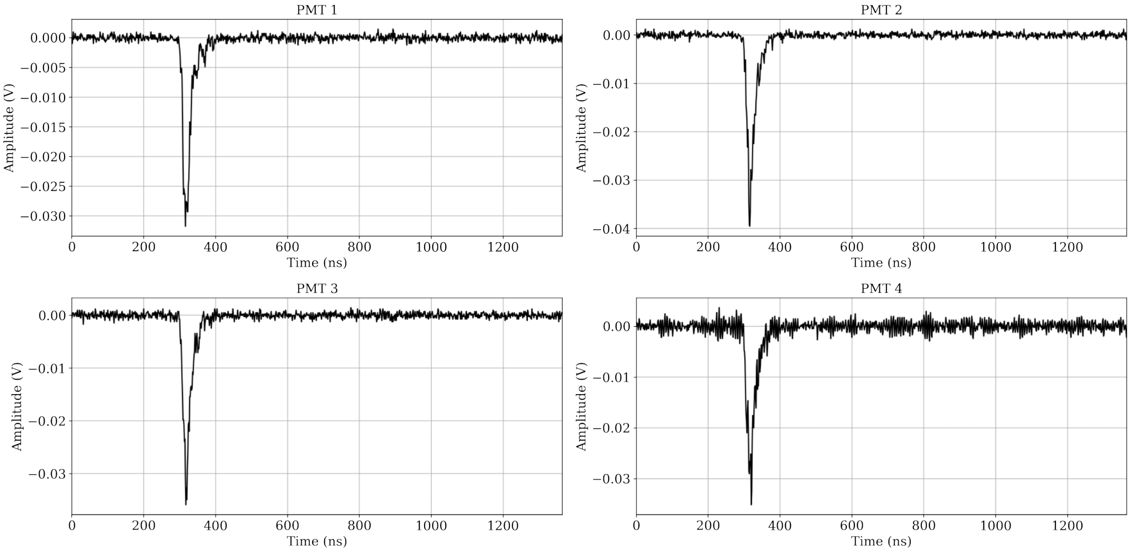

(b) Simulated waveforms of the Fast Digitizer.

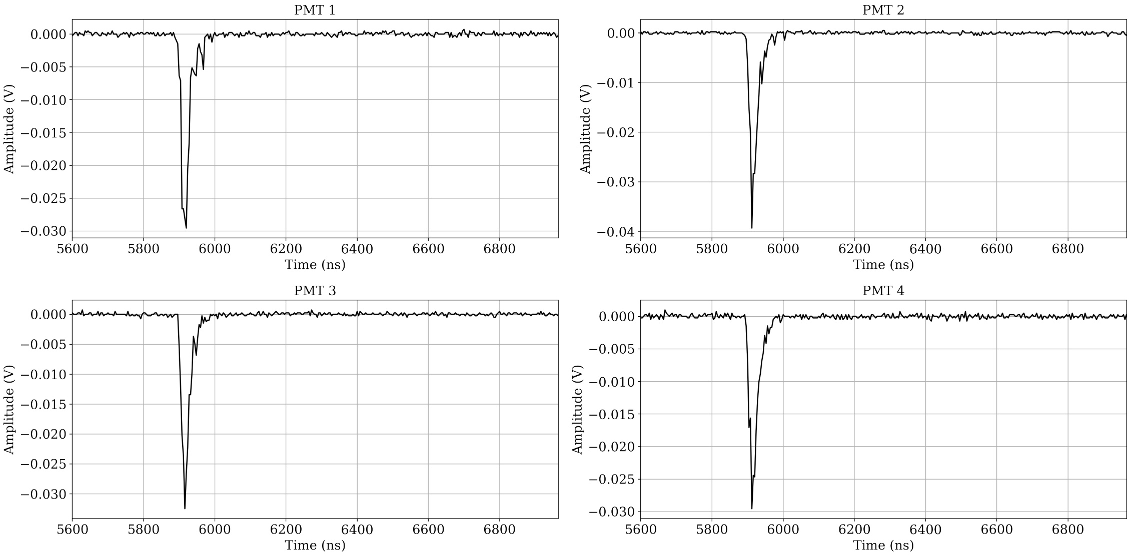

(c) Simulated waveforms of the Slow Digitizer.

Source: Prepared by the author (2024).

Figure 41 – Simulation example 2: Centered ^{55}Fe spot, z position = 466 mm

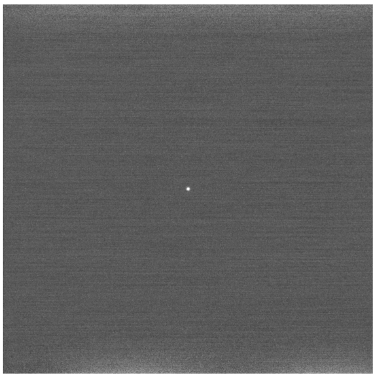

(a) Simulated image.

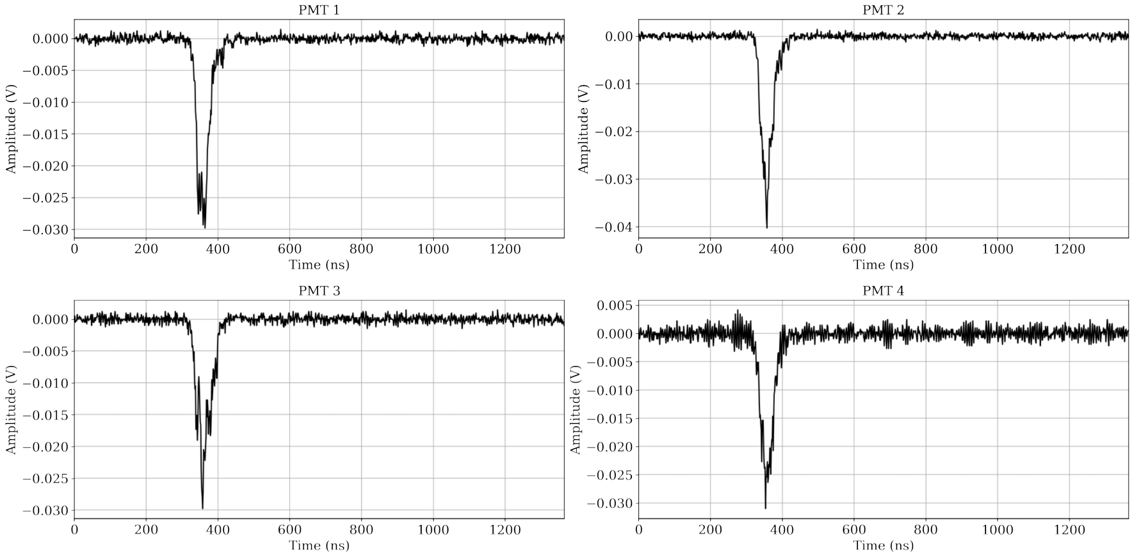

(b) Simulated waveforms of the Fast Digitizer.

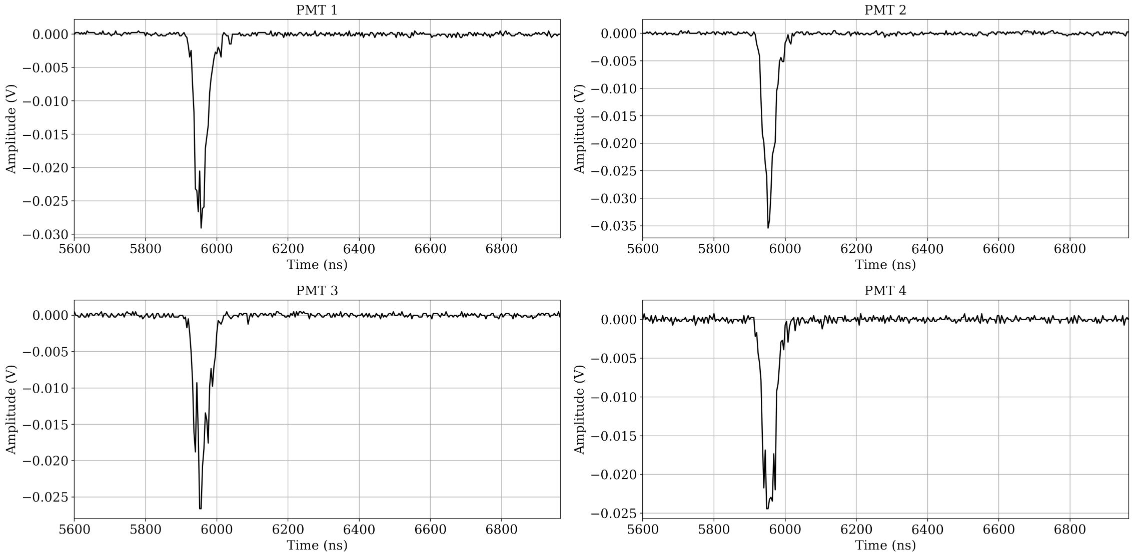

(c) Simulated waveforms of the Slow Digitizer.

Source: Prepared by the author (2024).

Figure 42 – Simulation example 3: ^{55}Fe spot on top of the PMT 1, z position = 50 mm

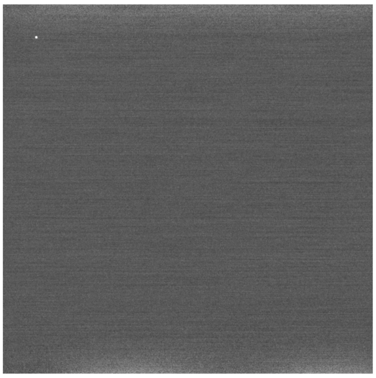

(a) Simulated image.

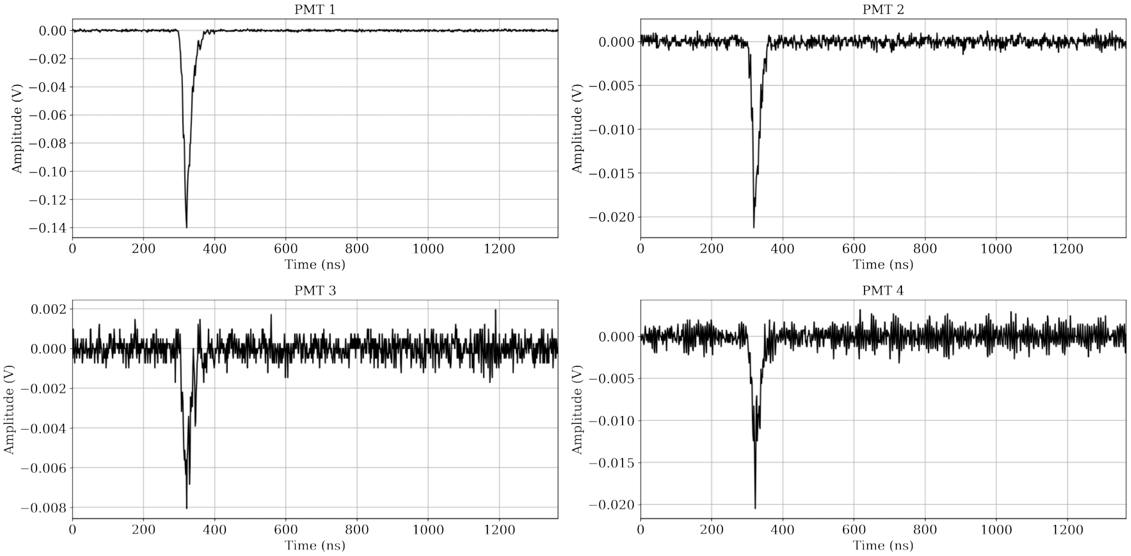

(b) Simulated waveforms of the Fast Digitizer.

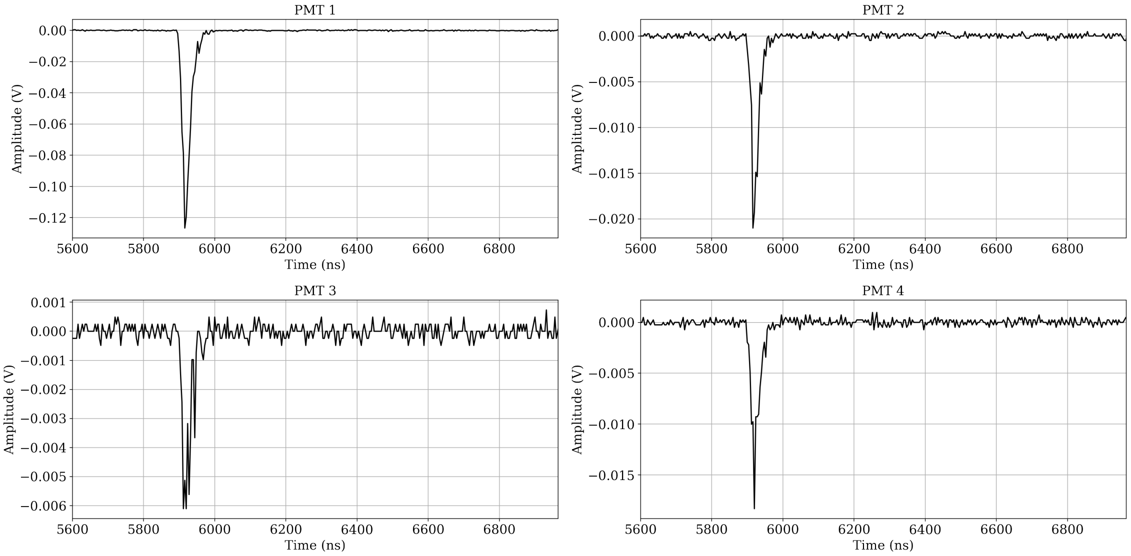

(c) Simulated waveforms of the Slow Digitizer.

Source: Prepared by the author (2024).

Figure 43 – Simulation example 4: ^{55}Fe spot on top of the PMT 1, z position = 466 mm

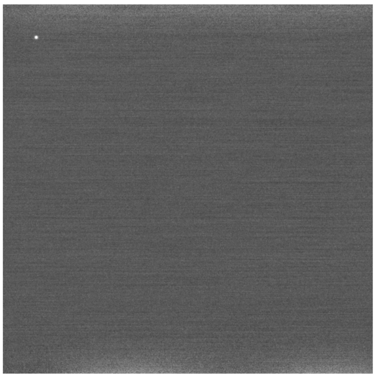

(a) Simulated image.

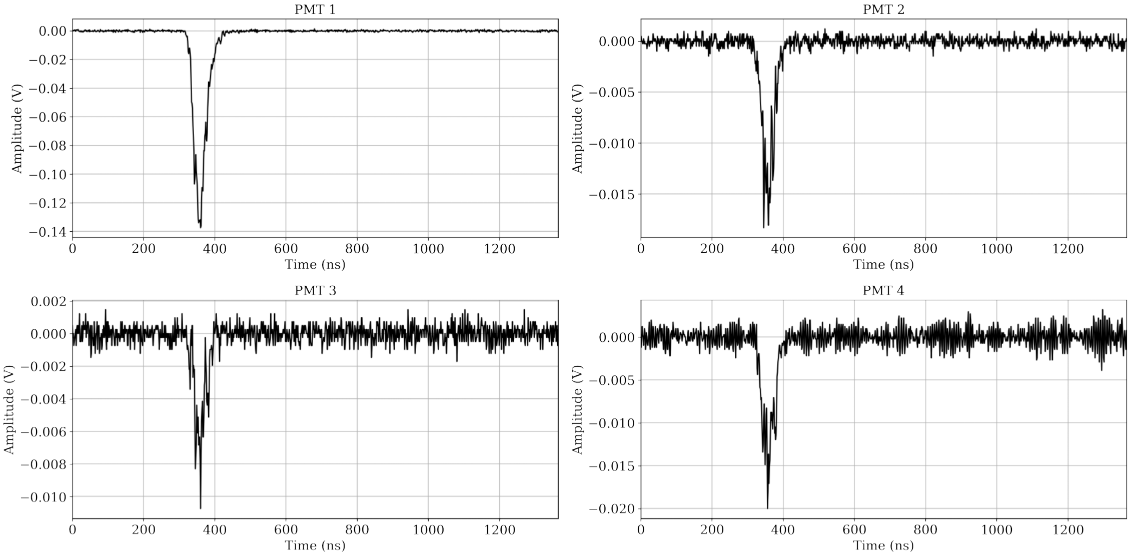

(b) Simulated waveforms of the Fast Digitizer.

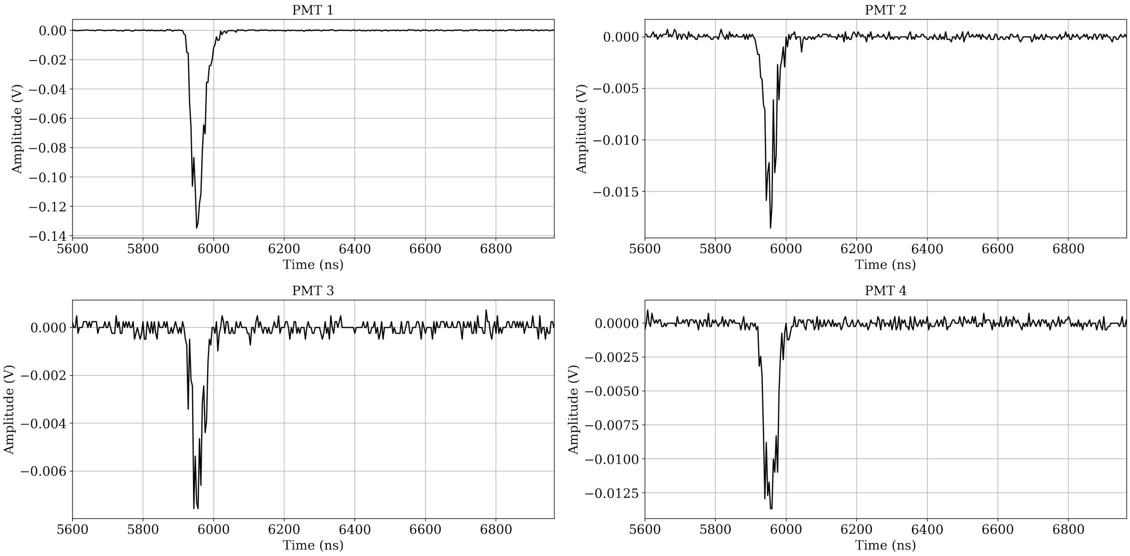

(c) Simulated waveforms of the Slow Digitizer.

Source: Prepared by the author (2024).

Figure 44 – Simulation and data comparison for z = 50 mm (Step 1)

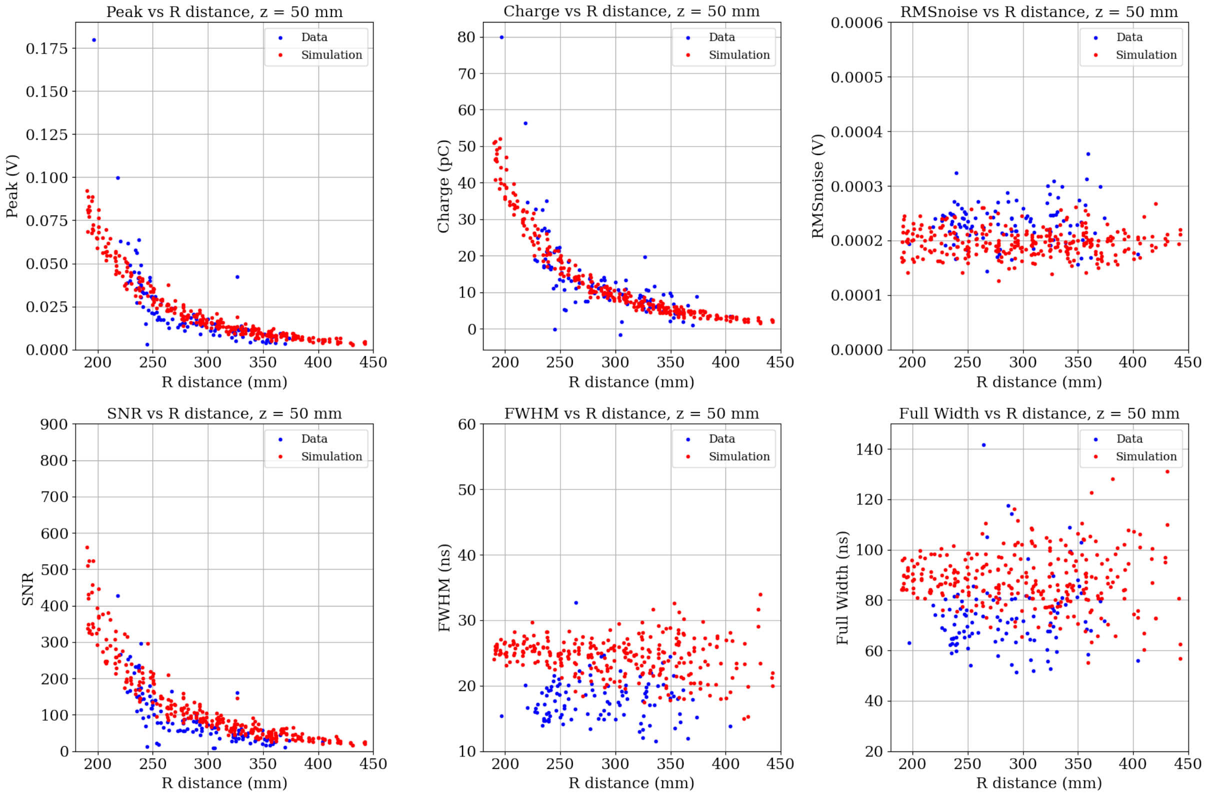

Source: Prepared by the author (2024).

Figure 45 – FWHM and Full Width at the Baseline in function of the z distance from the GEM plane.

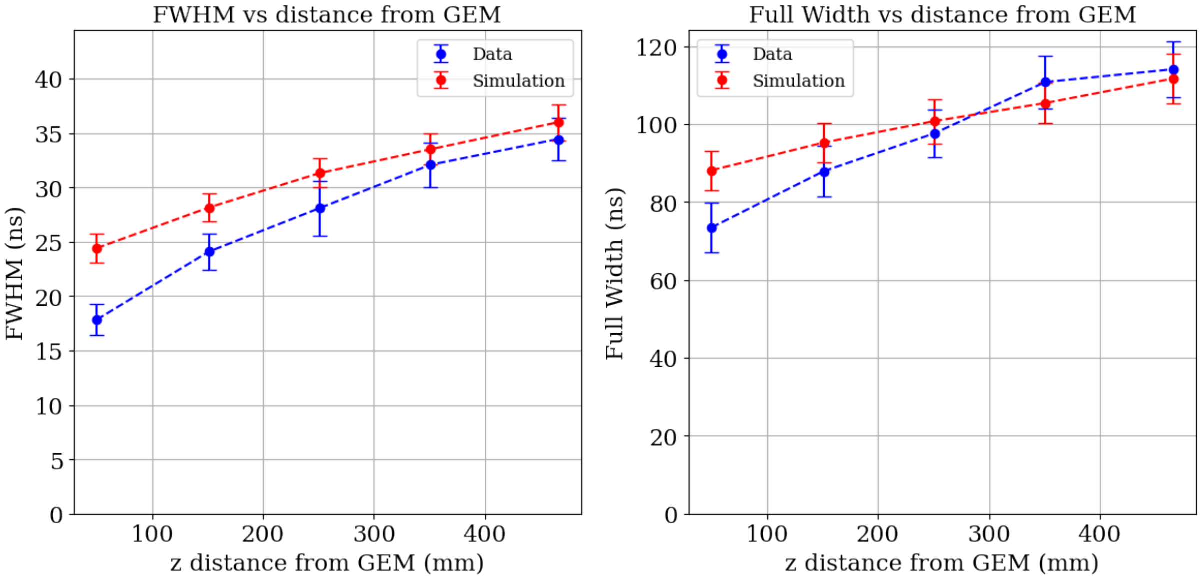

Source: Prepared by the author (2024).

7 CONCLUSION

This work successfully developed and validated a comprehensive model for simulating PMT signals in the CYGNO experiment. By accurately characterizing SPE signals and electronic noise, the simulation provides a realistic representation of the waveforms observed in experimental setups. The characterization of electronic noise and its simulation showed a high degree of agreement, reinforcing the reliability of this aspect of the methodology. However, when comparing the overall simulation with real data, some differences were observed, indicating the need for further refinements.

The most significant discrepancies were noted in the FWHM and Full Width at the Baseline, revealing that the main issue lies in the spread of the signal. This suggests that a more in-depth study on temporal dispersion is necessary to better understand and address these differences.

Moreover, the PMT simulation plays a crucial role in ongoing studies investigating the association between signal spots detected in the sCMOS image and their corresponding PMT waveforms. This analysis marks the starting point for deeper studies on the three-dimensional reconstruction of particle trajectories, as well as event selection and background rejection. Since a single image may contain multiple events, establishing this association is essential for the accurate analysis of the data.

Looking ahead, the next phase of the CYGNO project, PHASE_1, will involve the construction of CYGNO-04, which will feature a greater number of PMTs arranged in a different configuration compared to the LIME prototype. As a result, further improvements and adaptations of the simulation will be necessary to support future analyses, making this an important direction for ongoing and future research. Additionally, future work is expected to involve simulating more ^{55}Fe events within a single image, as the present study only considered one spot per image. Another crucial development is the simulation of different types of events with varying energies, such as long tracks, which differ from the circular shape characteristic of ^{55}Fe interactions. These enhancements will contribute to a more comprehensive and flexible simulation framework, further improving the accuracy of data analysis in the CYGNO experiment.

REFERENCES

1 AMARO, F. D. et al. The CYGNO Experiment. **Instruments**, v. 6, n. 1, p. 6, 2022.

2 JUNGMAN, G.; KAMIONKOWSKI, M.; GRIEST, K. Supersymmetric dark matter. **Physics Reports**, 267(5), 195-373, 1996.

3 KIBBLE, T. W. The standard model of particle physics. **European Review**, Cambridge University Press, v. 23, n. 1, p. 36–44, 2015.

4 LIU, J.; CHEN, X.; JI, X. Current status of direct dark matter detection experiments. **Nature Physics**, Nature Publishing Group, v. 13, n. 3, p. 212–216, 2017.

5 BERTONE, G.; HOOPER, D.; SILK, J. Particle dark matter: Evidence, candidates and constraints. **Physics reports**, Elsevier, v. 405, n. 5-6, p. 279–390, 2005.

6 BOND, J. R; EFSTATHIOU, G.; SILK, J. Massive neutrinos and the large-scale structure of the universe. **Physical Review Letters**, APS, v. 45, n. 24, 1980.

7 ELLIS, J. et. al. **Supersymmetric relics from the big bang**. 1984.

8 SIKIVIE, P. Dark matter axions. **International Journal of Modern Physics A**, World Scientific, v. 25, n. 02n03, p. 554-563, 2010.

9 PRESKILL, J.; WISE, M. B.; WILCZEK, F. Cosmology of the invisible axion. **Physics Letters B**, Elsevier, v. 120, n. 1-3, p 127-132, 1983.

10 DODELSON, S.; WIDROW, L. M. Sterile neutrinos as dark matter. **Physical Review Letters**, APS, v. 72, n. 1, p 17, 1994.

11 COSTA, Igor Abritta. **Optimization of the clustering algorithm of the CYGNO experiment**. Thesis (Doctorate) - Universidade Federal de Juiz de Fora, Faculty of Engineering. Post-Graduation Program in Electrical Engineering, 2020.

12 APRILE, E. et al. Dark matter results from 225 live days of XENON100 data. **Physical Review Letters**, APS, v. 109, n. 18, p 181301, 2012.

13 AHLEN, S. et al. Limits on cold dark matter candidates from an ultralow background germanium spectrometer. **Physics Letters B**, Elsevier, v. 195, n. 4, p. 603-608, 1987.

14 AGUILAR-AREVALO, A. et al. Search for low-mass WIMP in a 0.6 kg day exposure of the DAMIC experiment at SNOLAB. **Physical Review D**, APS, v. 94, n. 8, p. 082006, 2016.

15 CRISLER, M. et al. SENSEI: first direct-detection constraints on sub-GeV dark matter from a surface run. **Physical Review Letters**, APS, v. 121, n. 6, p. 061803, 2018.

16 BERNABEI, R. et al. First model independent results from DAMA/LIBRA-phase2. **Universe**, Multidisciplinary Digital Publishing Institute, v. 4, n. 11, p. 116, 2018.

17 PARK, J. Status of the COSINE Experiment. In: **Proceedings, 12th Patras Workshop on Axions, WIMPs and WISPs (PATRAS 2016): Jeju Island, South Korea**. [S.l.: s.n.], 2016, p. 125-128.

18 ASHCROFT, N. W.; MERMIN, N. D. **Solid State Physics**. 1976.

19 BRONIATOWSKI, A. et al. Cryogenic Ge detectors with interleaved electrodes: Design and modeling. **Journal of Low Temperature Physics**, Springer, v. 151, n. 3-4, p. 830-834, 2008.

20 AKERIB, D. et al. Surface Event Rejection Using Phonon Information in CDMS. **Nuclear Physics B-Proceedings Supplements**, Elsevier, v. 173, p. 137-140, 2007.

21 AGNES, P. et al. Results from the first use of low radioactivity argon in a dark matter search. **Physical Review D**, APS, v. 93, n. 8, p. 081101, 2016.

22 AMAUDRUZ, P.-A. et al. Measurement of the scintillation time spectra and pulse-shape discrimination of low-energy β and nuclear recoils in liquid argon with DEAP-1. **Astroparticle Physics**, Elsevier, v. 85, p. 1-23, 2016.

23 AKERIB, D. S. et al. First results from the LUX dark matter experiment at the Sanford Underground Research Facility. **Physical Review Letters**, APS, v. 112, n. 9, p. 091303, 2014.

24 ANGLE, J. et al. Search for light dark matter in XENON10 data. **Physical Review Letters**, APS, v. 107, n. 5, p. 051301, 2011.

25 AUBIN, F. et al. Discrimination of nuclear recoils from alpha particles with superheated liquids. **New Journal of Physics**, IOP Publishing, v. 10, n. 10, p. 103017, 2008.

26 BARNABÉ-HEIDER, M. et al. Response of superheated droplet detectors of the PICASSO dark matter search experiment. **Nuclear Instruments and Methods in Physics Research Section A: Accelerators, Spectrometers, Detectors and Associated Equipment**, Elsevier, v. 555, n. 1-2, p. 184-204, 2008.

27 AMOLE, C. et al. Improved dark matter search results from PICO-2L Run 2. **Physical Review D**, APS, v. 93, n. 6, p. 061101, 2016.

28 AMOLE, C. et al. Dark matter search results from the PICO-60 CF_3I bubble chamber. **Physical Review D**, APS, v. 93, n. 5, p. 052014, 2016.

29 BOLTE, W. et al. A bubble chamber for dark matter detection (the COUPP project status). In: IOP PUBLISHING. **Journal of Physics: Conference Series**. [S.l.], 2006, v. 39, n. 1, p. 126.

30 SANTOS, D. et al. MIMAC: MIcro-tpc MAtrix of Chambers for dark matter directional detection. In: **J. Phys. Conf. Ser.**, [S.l.], 2013, v. 469, n. 012002, p. 1311-0616.

31 BATTAT, J. et al. Low threshold results and limits from the DRIFT directional dark matter detector. **Astroparticle Physics**, Elsevier, v. 91, p. 65-74, 2017.

32 NYGREN, D. R. **The time projection chamber**. 1978.

33 SAULI, F. Micro-pattern gas detectors. **Nuclear Instruments and Methods in Physics Research Section A: Accelerators, Spectrometers, Detectors and Associated Equipment**, Elsevier, v. 477, n. 1-3, p. 1-7, 2002.

34 GOMEZ-CADENAS, J. J.; CAPILLA, F. M.; FERRARIO, P. High pressure gas xenon tpcs for double beta decay searches. **Frontiers in Physics**, Frontiers, p. 51, 2019.

35 BARACCHINI, E. Stability and detection performance of a GEM-based Optical Readout TPC with He/CF4 gas mixtures. **Journal of Instrumentation**, Frontiers, v.15, n. 10, p. P10001, 2020.

36 SAULI, F. Gem: A new concept for electron amplification in gas detectors. **Nuclear Instruments and Methods in Physics Research Section A: Accelerators, Spectrometers, Detectors and Associated Equipment**, Elsevier, v. 386, n. 2-3, p. 531–534, 1997.

37 BACHMANN, S. et al. Development and applications of the gas electron multiplier. **Nuclear Instruments and Methods in Physics Research Section A: Accelerators, Spectrometers, Detectors and Associated Equipment**, Elsevier, v. 471, n. 1-2, p. 115-119, 2001.

38 MARINHO, P. R. B. **Desenvolvimento de detectores Sensíveis à posição Multifilares e Multi-GEM para Obtenção de Imagens de Raios-X**. Tese (Doutorado) - Tese de Doutorado, CBPF. Rio de Janeiro, 2006.

39 ALTUNBAS, C. et al. Construction, test and commissioning of the triple-gem tracking detector for compass. **Nuclear Instruments and Methods in Physics Research Section A: Accelerators, Spectrometers, Detectors and Associated Equipment**, Elsevier, v. 490, n. 1-2, p. 177–203, 2002.

40 ALFONSI, M. et al. High-rate particle triggering with triple-gem detector. **Nuclear Instruments and Methods in Physics Research Section A: Accelerators, Spectrometers, Detectors and Associated Equipment**, Elsevier, v. 518, n. 1-2, p. 106–112, 2004.

41 LAMI, S. et al. A triple-gem telescope for the totem experiment. **Nuclear Physics B-Proceedings Supplements**, Elsevier, v. 172, p. 231–233, 2007.

42 HAMAMATSU PHOTONICS. **PMT Handbook: Basics and Applications**. 4th ed. Japan: Hamamatsu Photonics K.K., 2017.

43 ABDALLA, E., et al. Cosmology Intertwined: A Review of the Particle Physics, Astrophysics, and Cosmology Associated with the Cosmological Tensions and Anomalies. **Journal of High Energy Astrophysics**, v. 34, p. 49-211, 2022.

44 ARONS, A. B.; PEPPARD, M. Einstein's proposal of the photon concept-a translation of the annalen der physik paper of 1905. **American Journal of Physics**, American Association of Physics Teachers, v. 33, n. 5, p. 367–374, 1965

45 HAMAMATSU PHOTONICS K.K. **Photomultiplier Tube R7378A Datasheet**.

46 FOLCARELLI, Matteo. **Characterization of the CYGNO experiment prototype during the underground campaign at LNGS**. Tesi di Laurea Magistrale. Sapienza University of Rome, 2023.

47 CAEN S.p.A. **Mod. V1742 32+2 Channel 12bit 5 GS/s Switched Capacitor Digitizer**.

48 CAEN S.p.A. **Mod. V1720 8 Channel 12bit - 250MS/s Digitizer**.

49 CYGNUS-RD Collaboration. **Digitization Repository**. Available at: `https://github.com/CYGNUS-RD/digitization`.

50 BORRA, Francesco. **Study of the PMTs signals during the first underground run of the LIME prototype for the CYGNO experiment**. Master's thesis. Sapienza – University of Rome, 2022.

51 MARTINI, P.; MIGLIORATI, D.; MUCO, G.; ZAPPATERRA, L., **Physics Laboratory II report**, CYGNO LAB GROUP, 2022.

52 PURUSHOTHAMAN, S. et al. Hyper-EMG: A new probability distribution function composed of Exponentially Modified Gaussian distributions to analyze asymmetric peak shapes in high-resolution time-of-flight mass spectrometry. **International Journal of Mass Spectrometry**, v. 421, p. 245–254, 2017.

53 VASEGHI, Saeed V. **Advanced Digital Signal Processing and Noise Reduction**. 2. ed. Chichester: John Wiley & Sons, 2000.

54 MARPLE, S. L.**Digital spectral analysis with applications**. Prentice-Hall, 1987

55 STOICA, P.; MOSES, R. L. **Spectral analysis of signals**. Prentice-Hall, 2005.

56 KAY, S. M.; MARPLE, S. L. Spectrum analysis—A modern perspective. **Proceedings of the IEEE**, v. 69, n. 11, p. 1380-1419, 1981.

57 SCHUSTER, A. On the investigation of hidden periodicities with application to a supposed 26 day period of meteorological phenomena. **Terrestrial Magnetism**, v. 3, p. 13-41, 1898.

58 BARTLETT, M. S. Smoothing Periodograms from Time-Series with Continuous Spectra. **Nature**, v. 161, p. 686–687, 1948.

59 WELCH, P. D. The use of fast Fourier transform for the estimation of power spectra: A method based on time averaging over short, modified periodograms. **IEEE Transactions on Audio and Electroacoustics**, v. 15, p. 70-73, 1967.

60 HARRIS, F. J. On the use of windows for harmonic analysis with the discrete Fourier transform. **Proceedings of the IEEE**, v. 66, p. 51-83, 1978.

61 VIRTANEN, P et al. SciPy 1.0: Fundamental Algorithms for Scientific Computing in Python. **Nature Methods**, v. 17, p. 261-272, 2020.

62 SMAINI, Lydi. **RF Analog Impairments Modeling for Communication Systems Simulation: Application to OFDM-based Transceivers**. Chichester: John Wiley & Sons, 2012.

63 TELEDYNE LECROY. **WaveSurfer 4000HD Datasheet**. Available at: `https://cdn.teledynelecroy.com/files/pdf/wavesurfer-4000hd-datasheet.pdf`.

64 KNOLL, Glenn F. **Radiation Detection and Measurement** (4th ed.). 2010.

65 JUNG, Bouke. **PMT Signal Processing**. 2023.

66 KISSICK, David J.; MUIR, Ryan D.; SIMPSON, Garth J. Statistical Treatment of Photon/Electron Counting: Extending the Linear Dynamic Range from the Dark Count Rate to Saturation. **Analytical Chemistry**, v. 82, n. 24, p. 10129–10134, 2010.

67 JETTER, G. J.; HUANG, Y. B.; CHANG, J. F.; CHENG, Y. P.; CHEN, Z. W.; HU, J.; JI, X. L.; LI, F.; LI, J.; LI, Q. J.; QIAN, X.; WANG, W.; XU, Y.; YU, Z. Y.; ZHANG, Z. W. PMT Waveform Modeling at the Daya Bay Experiment. **Chinese Physics C**, v. 36, n. 8, p. 733–738, 2012.

68 GAFRILLER, Judith. Characterizing PMT pulses for IceCube. **DESY Summer Student Programme**, 2018.

APPENDIX A – Results of the Comparative Analysis Between Real and Simulated Data

Figure 46 – Simulation and data comparison for z = 151 mm (Step 2)

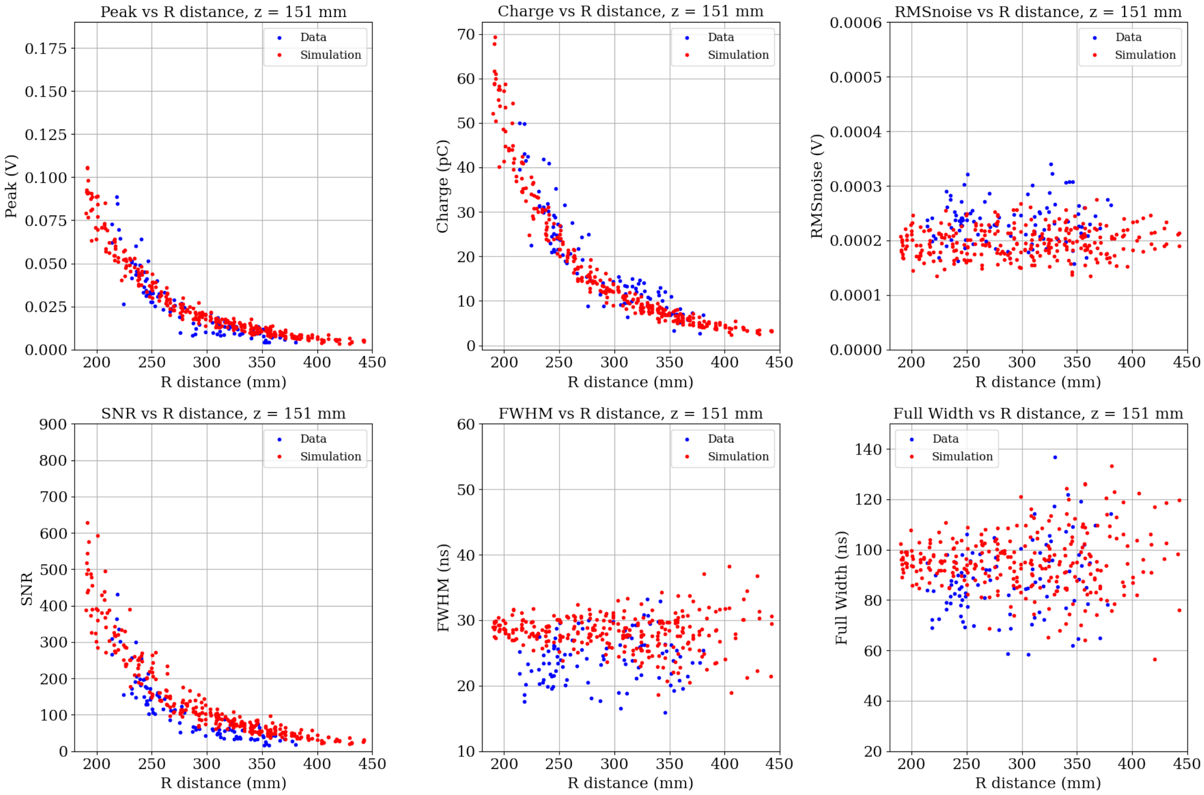

Source: Prepared by the author (2024).

Figure 47 – Simulation and data comparison for z = 251 mm (Step 3)

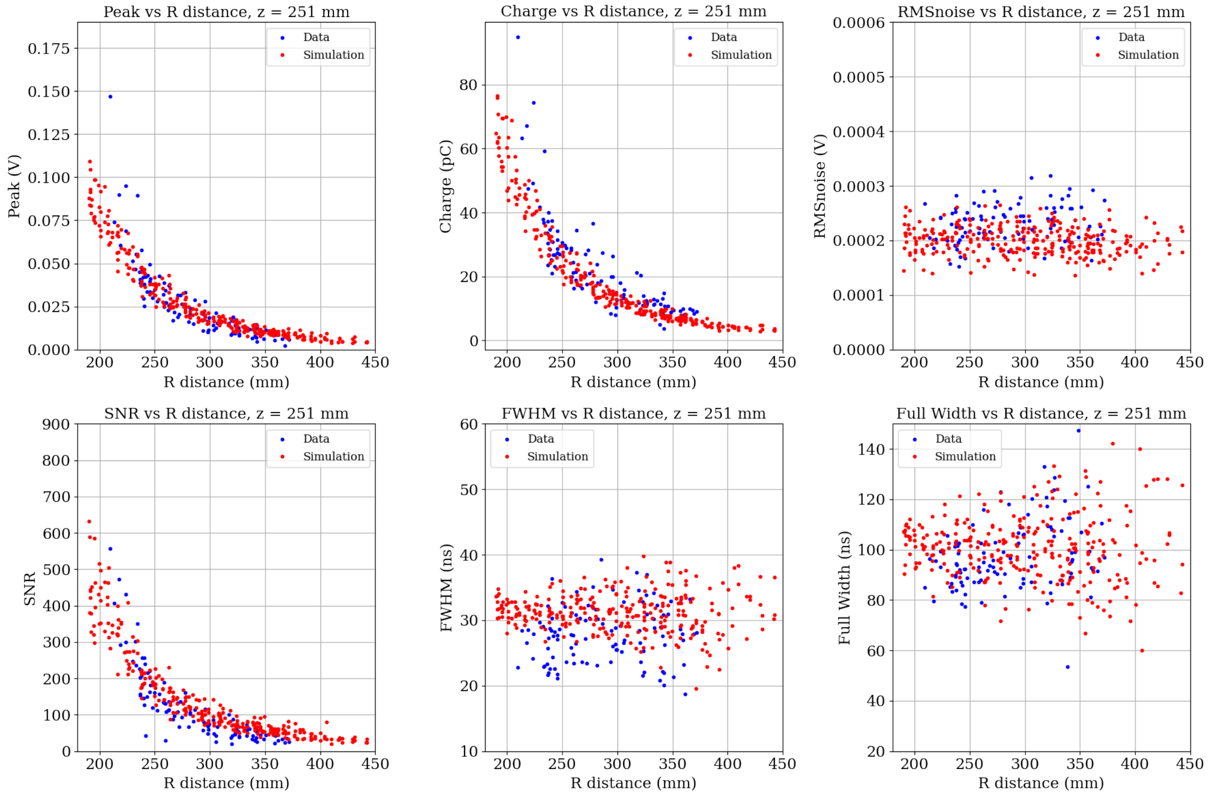

Source: Prepared by the author (2024).

Figure 48 – Simulation and data comparison for z = 351 mm (Step 4)

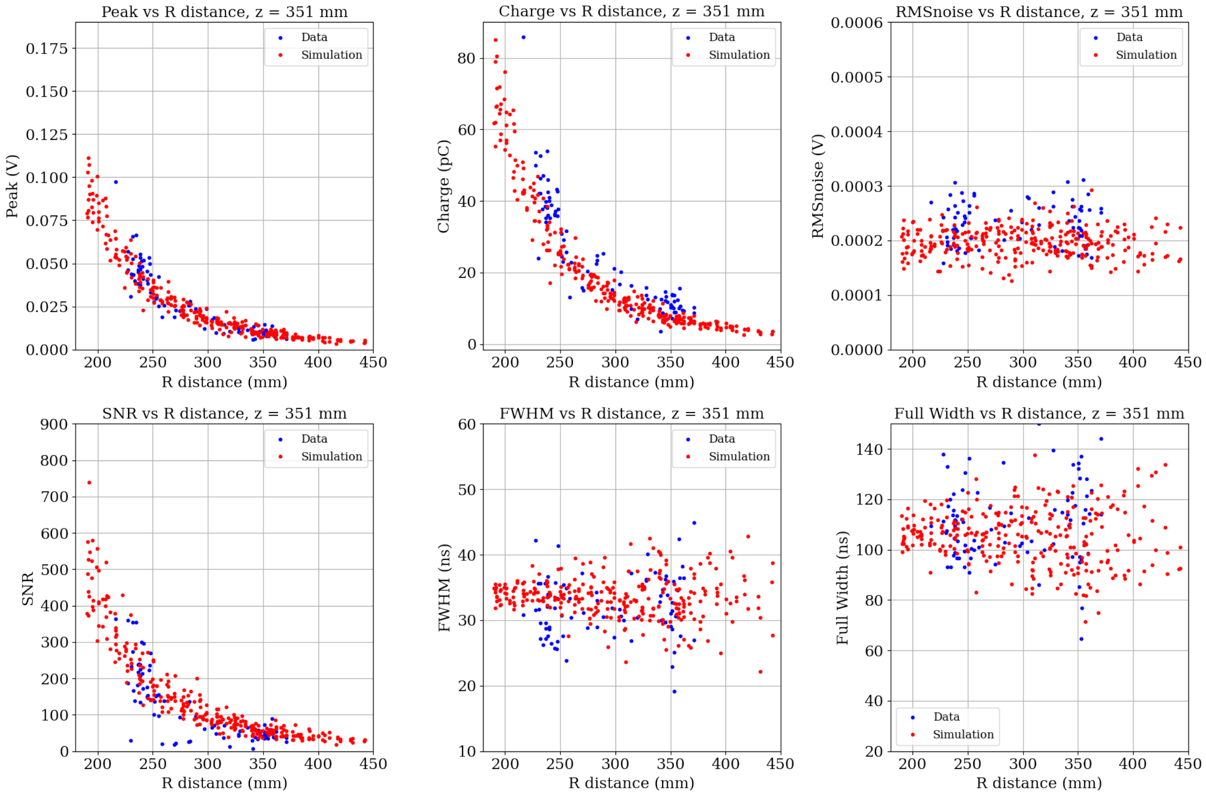

Source: Prepared by the author (2024).

Figure 49 – Simulation and data comparison for z = 466 mm (Step 5)

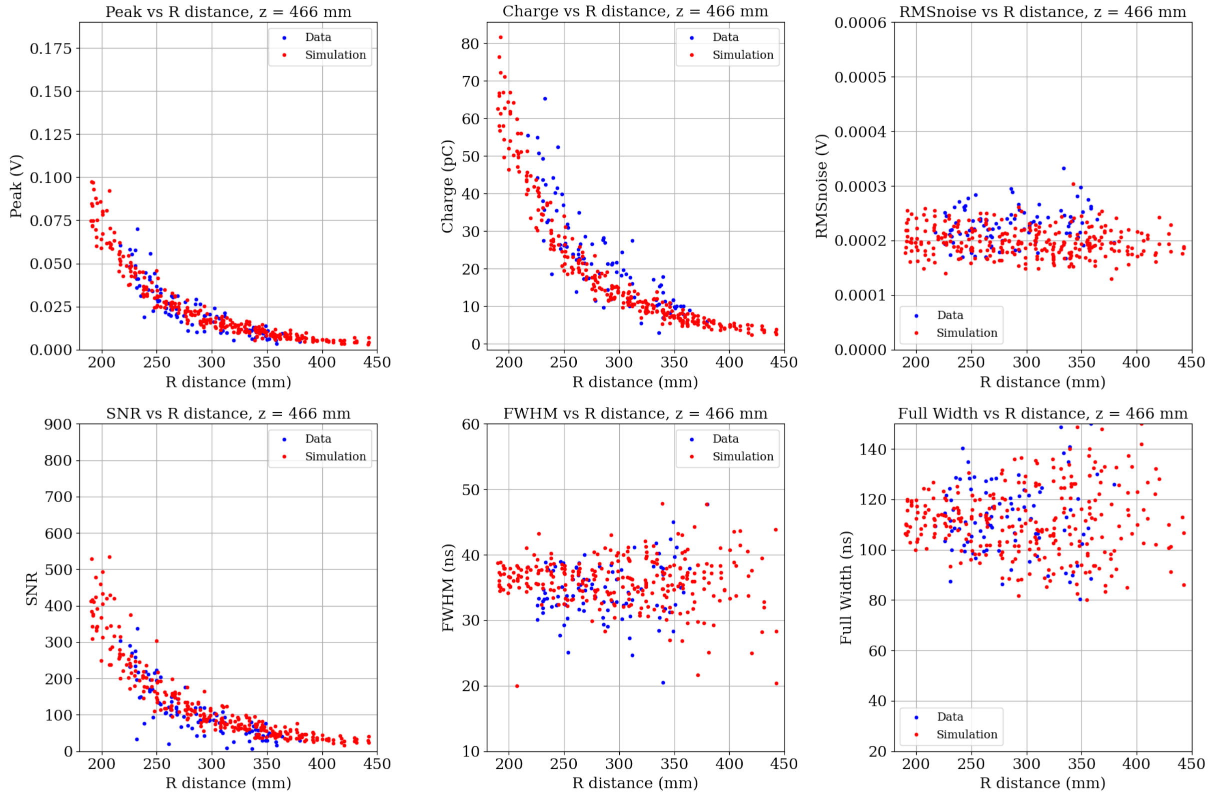

Source: Prepared by the author (2024).